

Department of Mechanical and Aerospace Engineering

Master's Thesis in Mechanical Engineering

# **Experimental Analysis of Nonlinear Piezoelectric Systems for Vibration Energy Harvesting**

Supervisors:

Student:

Dario Anastasio

Mingjie Chen

Alessandro Paolo Daga

#### **Abstract**

Nonlinear vibration energy harvesting (VEH) offers distinct advantages over conventional linear harvesters, particularly in addressing the narrowband limitation inherent in resonance-based systems. By intentionally introducing nonlinear mechanisms, these devices can achieve improved energy conversion efficiency, broader operational bandwidth, and greater adaptability to environmental variability.

Among nonlinear approaches, stopper-based configurations—also referred to as motion limiters—provide a practical method to generate piecewise nonlinear stiffness. In theory, properly designed stoppers induce hardening effects, suppress excessive displacements, and enable energy harvesting across multiple frequency bands. However, practical realization remains challenging, as stopper dynamics themselves may contribute unintended resonances and energy exchanges not accounted for in simplified models.

This thesis investigates stopper-integrated cantilever piezoelectric systems through numerical modelling and experimental testing. Initially, a nonlinear lumped-parameter model is established and solved using state-space and Newmark- $\beta$  integration methods, with the stopper represented as a high-stiffness element. Simulations predicted clear hardening behavior and bandwidth enhancement.

Experimental results, however, revealed discrepancies. The 3D-printed stoppers are significantly more flexible than predicted by CAD simulations, introducing their own resonance frequencies close to the cantilever's first mode. This unexpected interaction suppressed the anticipated hardening effect and instead caused energy exchange between beam and stopper. These findings highlight the limitations of simplified stopper models and the need to account for the dynamic behavior of limiter structures.

Building on this analysis, the thesis proposes directions for a redesigned test setup, including more rigid stopper geometries, alternative mounting orientations, and potential horizontal shaker implementation. The outcomes contribute both practical insight into stopper realization and theoretical refinement of nonlinear VEH modelling strategies.

## Contents

1.Introduction	1
1.1 Overview and Advantages of Vibration Energy Harvesting (VEH)	1
1.2 Technical Challenges and Classification of VEH Systems	2
1.3 State of the Art about VEH Systems	3
1.4 Nonlinear Piezoelectric System in Cantilever Beam with Mass	4
2. System Modelling and Methodology	6
2.1 Physical System Specifications	6
2.1.1 Harvesting Device Configuration	7
2.1.2 Stopper Design and Parameterization	8
2.2 Mathematical Model	11
2.2.1 Modelling of the Linear System (with Piezoelectric Coupling)	11
2.2.2 Nonlinear Stopper Model	12
2.2.3 Complete Nonlinear System Equations	14
2.3 Numerical Solution Method	15
2.3.1 Initial Approach: State Space Method	15
2.3.2 Enhanced Solution: Newmark Integrator	15
2.4 Model Objectives	18
3. Numerical Simulation	19
3.1 Introduction	19
3.2 Stopper Stiffness Estimation	19
3.2.1 Material Properties and Boundary Conditions	19
3.2.2 Stiffness estimation	20
3.3 Linear System Benchmark Validation	22
3.3.1 Natural Frequency and Damping Validation	22
3.3.2 Frequency Response of the Linear System under Harmonic Excitation	23

3.4 State-Space Method: Discontinuity-Induced Divergence	25
3.5 Newmark-β Method: Implementation and Convergence Analysis	27
3.5.1 Stiffness Optimization after Experimental Limitations	27
3.5.2 Random Excitation and Broadband Validation	28
3.5.3 Numerical Outputs and Convergence Considerations	30
3.6 Error and Convergence Analysis	36
4. Experimental Tests	37
4.1 Linear experimental setup and measurement system	37
4.2 First experimental setup and measurement system	42
4.2.1 Stiffness Optimization and Redesigned Stopper	44
4.3 Experimental Reconfiguration and Motivation	45
4.3.1 Design Concept of the Semi-Cylindrical Stopper	47
4.4 Nonlinear Experimental Validation	49
4.4.1 Random Excitation Tests	53
4.4.2 Frequency-Sweep Excitation Tests	57
4.4.3 Discussion	60
5. Conclusion	62
6. Reference	64

## 1.Introduction

## 1.1 Overview and Advantages of Vibration Energy Harvesting (VEH)

With the development of technology, energy harvesting has found increasingly widespread applications. Vibration Energy Harvesting emerged as a highly promising method that converts ambient mechanical vibrations into electrical energy(1,2). This method has many unique advantages, especially for low-power electronic devices such as self-powered sensors(3).

Compared with traditional chemical batteries, vibration energy harvesting offers a promising alternative in numerous applications, leading to significant cost savings and mitigating issues such as limited lifespan and the need for frequent charging or replacement associated with conventional power sources(1,4). Furthermore, this approach avoids the environmental contamination caused by battery disposal(5). Additionally, by harnessing ambient vibrations and converting mechanical energy into electricity, vibration energy harvesting enables operational independence from fixed power infrastructure, providing autonomous functionality(6). As a method utilizing ever-present environmental vibrations, it represents a renewable and sustainable energy strategy that not only reduces reliance on conventional batteries but also helps lower carbon emissions, contributing positively to environmental protection(4).

Furthermore, ambient vibrations represent an abundant and readily available energy source, making vibration energy harvesting (VEH) exceptionally convenient for practical implementation(7). More significantly, VEH systems eliminate dependency on external power supplies while simultaneously enhancing data accessibility and connectivity(4). These unique characteristics enable reliable operation of electronic devices in challenging environments, particularly for self-powered sensors, Internet of Things (IoT) networks, and various low-power electronic applications(1,8).

In IoT systems where sensors often operate in extreme conditions - such as ocean buoy sensors that convert wave vibrations into electricity - VEH technology provides a groundbreaking self-sustaining solution(9). This innovative approach has transformed the energy landscape by offering an autonomous, sustainable power alternative for low-power devices and sensor networks, completely independent of traditional energy sources(10). This transformative potential positions VEH as a key enabler for the next generation of self-sustaining electronic systems(11).

## 1.2 Technical Challenges and Classification of VEH Systems

Although Vibration Energy Harvesting (VEH) presents considerable advantages, its widespread practical application is challenged by the random and broadband nature of ambient vibrations(12). The main challenge is the limited working bandwidth - effective energy conversion requires environmental vibration to occur in a narrow band near the resonant frequency of the harvester. However, environmental vibrations usually exhibit wide-spectrum characteristics, which often exceed the optimal bandwidth, resulting in a significant reduction in energy extraction efficiency.

Moreover, the random and wideband characteristics of most environmental vibrations often lead to poor harvester performance, and sometimes even cause the system to fail to meet operating requirements. Therefore, extending the effective working bandwidth has become a key research focus to improve VEH efficiency(3).

Vibration energy harvesting technologies are primarily based on three working principles:

- Piezoelectric (direct conversion of mechanical stress to charge),
- **Electromagnetic** (induction via relative motion in magnetic fields),
- Electrostatic (capacitance variation from moving electrodes).

These methods have attracted significant attention due to their efficient energy conversion mechanisms and diverse application scenarios(1,2).

In this study, the piezoelectric energy harvesting approach is adopted. This technology utilizes the direct piezoelectric effect of piezoelectric materials, which can directly generate electric potential under mechanical stress, thereby converting mechanical vibration energy into electrical energy. It is particularly suitable for environmental vibration energy harvesting applications.

## 1.3 State of the Art about VEH Systems

To broaden the operating bandwidth of vibration energy harvesters (VEHs), researchers have proposed various strategies. Multimodal techniques achieve this by designing structures with multiple closely spaced resonant peaks (e.g., multi-degree-of-freedom (M-DOF) systems, L-shaped beams, or "cut-out" beams)(12). Nonlinear techniques exploit magnetic coupling or geometric buckling to introduce monostable, bistable, or even multistable characteristics, enabling broadband responses through large-amplitude intra-well or inter-well nonlinear oscillations. Frequency up-conversion (FUC) techniques aim to transform low-frequency ambient vibrations into high-frequency localized strain in piezoelectric materials, typically via mechanical impacts, thereby enhancing conversion efficiency(8).

However, these approaches face distinct challenges: Multimodal systems suffer from significant power attenuation in the "valleys" between resonant peaks, limiting overall efficiency across the intended bandwidth(12). Traditional nonlinear structures (e.g., bistable configurations) often require high excitation thresholds to trigger effective inter-well snap-through motion. Conventional FUC mechanisms, relying predominantly on instantaneous impacts for energy transfer, exhibit limitations in achievable efficiency and bandwidth potential(8).

To address these limitations, nonlinear piezoelectric systems for vibration energy harvesting utilizing impact-based 'stopper' mechanisms present a promising alternative. These systems leverage controlled physical collisions to introduce strong nonlinear dynamics, potentially enabling broadband responses at lower excitation levels while mitigating the inter-peak valley issue inherent in multimodal designs.

#### 1.4 Nonlinear Piezoelectric System in Cantilever Beam with Mass

This study develops a nonlinear piezoelectric energy harvesting system using stoppers in a tip-mass cantilever beam. As shown in Fig. 1, The core structure integrates piezoelectric materials (PZT) onto a steel cantilever beam with a concentrated end mass. Two stoppers are symmetrically placed above and below the tip mass, with their stiffness optimally designed to enable compliant deformation. An adjustable gap between the stoppers and the mass allows systematic investigation of gap-dependent nonlinear dynamics and energy harvesting performance. Experiments include comparisons of cases with/without piezoelectric materials to decouple mechanical nonlinearity from electromechanical coupling effects.

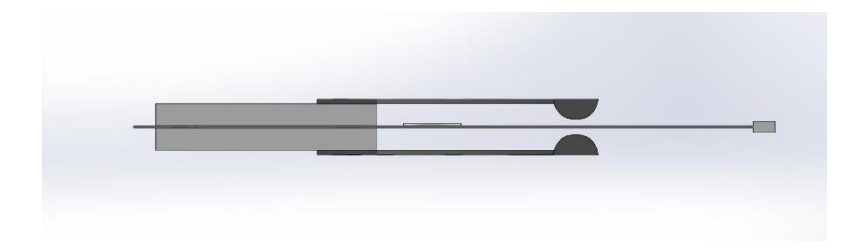


Figure 1.1. Tip-Mass Cantilever Beam with Stoppers and Piezoelectric

The stoppers create piecewise-linear stiffness variations to enhance bandwidth: contact at the gap threshold induces nonlinear stiffness switching, enabling energy harvesting across multiple frequency bands. The adjustable gap simultaneously provides an amplitude management—small gaps limit excessive displacements for device protection, while large gaps maintain sensitivity to minor vibrations.

This analysis aims to optimize the performance and explain the mechanisms of nonlinear piezoelectric vibration energy harvesting systems through experimental investigations of stoppers, while evaluating their potential for real-world applications. The study focuses on piecewise nonlinear dynamics induced by stoppers in a tip-mass cantilever system, employing systematic tests with adjustable gap parameters and comparative experiments with/without piezoelectric materials to quantify the contribution of impact nonlinearity to bandwidth enhancement and power amplification.

Building upon the research framework and motivations discussed above, the remainder of this thesis is structured as follows.

Chapter 2 (Modelling) presents the theoretical formulation of a nonlinear piezoelectric cantilever equipped with adjustable stoppers, introducing the electromechanical coupling model and the piecewise stiffness behavior associated with contact interactions.

Chapter 3 (Numerical Simulations) analyses the nonlinear dynamics through finite element and state-space approaches, identifying the influence of stopper stiffness and gap distance on

frequency response, energy transfer, and harvesting efficiency.

Chapter 4 (Experimental Validation) describes the realization of the redesigned prototype and the corresponding testing procedures under both random and frequency-sweep excitations. The measured responses confirm the presence of hardening-type nonlinearity and validate the predicted energy-harvesting trends.

Finally, Chapter 5 (Conclusions) summarizes the key findings, emphasizing the agreement between experimental and numerical results, the role of stopper compliance in shaping nonlinear behavior, and the practical insights gained for future optimization of vibration energy harvesting systems.

# 2. System Modelling and Methodology

This chapter systematically details the modelling theory and methodology for a piezoelectric energy harvesting (PEH) system integrated with an adjustable mechanical stopper. It begins by defining the key structural parameters and assembly relationships of the cantilever beam, piezoelectric transducer, and the stopper, based on physical system design specifications.

The core modelling effort focuses on establishing the system's nonlinear dynamic equations. The initial modelling approach employed the piecewise method to describe the cantilever's motion in both the linear vibration regime and the nonlinear regime where its motion is constrained by the stopper, intending to solve it using the state-space method. However, convergence issues arose due to discontinuities at the piecewise boundaries. To address this, the nonlinear contact force model is smoothed using a piecewise quadratic polynomial approximation, ensuring model validity without compromising experimental relevance.

A numerical solution framework based on the Newmark- $\beta$  integration method is developed to efficiently solve the resulting nonlinear equation by using MATLAB, and parametric analysis tasks are defined accordingly. For the stopper realization, SolidWorks is utilized for structural design and modelling, primarily to determine a geometric configuration achieving the desired stiffness characteristics. The final performance validation of the stopper is reserved for experimental testing.

The 3D model of the energy harvester was designed using SolidWorks Student Edition 2024 SP05. The dynamic equations were subsequently solved through numerical simulations performed in MATLAB R2024a.

The models and methods established in this chapter provide a solid theoretical foundation for subsequent numerical simulation studies and experimental validation.

## 2.1 Physical System Specifications

The experimental setup integrates four core subsystems:

- Cantilever beam structure (base energy harvesting platform)
- Piezoelectric transducers (mechanical-to-electrical conversion)
- Data acquisition infrastructure (performance quantification).
- Adjustable stopper mechanism (nonlinearity device)

System assembly ensures mechanical synchronization and parametric controllability for nonlinear dynamics investigation.

#### 2.1.1 Harvesting Device Configuration

The piezoelectric vibration energy harvesting system comprises the following key components:

#### Cantilever Beam Structure:

- Materials: Harmonic steel (Density: 7800 [kg/m^3]; Young's modulus E=200 [GPa])
- Dimensions: 170 mm (L)  $\times$  30 mm (W)  $\times$  1 mm (T)
- Tip Mass: 56.7 g rigidly bonded to free end (see Figure 2.1)
- Clamping: Rigid fixture by bolted connections in workstation

#### Piezoelectric Transducer:

- Materials: Ceramic with copper electrodes
- Dimensions:  $\emptyset$ 27 mm (D) × 0.4 mm (T)
- Position: 25 mm from clamped end
- Piezo circuit: Resistance 1  $M\Omega$  or 1  $k\Omega$  adding Voltage follower with LM741 operational amplifier (unity gain), powered by two 9V batteries to limit the output voltage between -9V and +9V.

#### Data acquisition infrastructure:

#### • Sensor Configuration:

Channel	Sensor type	Position	Model	Function
1	Base Accelerometer	0 mm	B&K 10423	Measure input excitation
2	Beam Accelerometer	50 mm	B&K 10545	Capture root vibrations
3	Beam Accelerometer	150 mm	B&K 10543	Capture free end vibrations
4	Piezo Voltage Sensor	25 mm		Record harvested energy

Table 1. Sensor Configuration

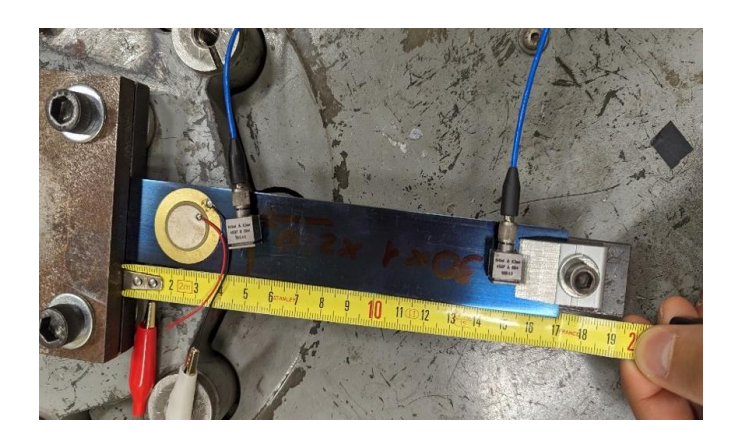


Figure 2.1: Harvesting Device Configuration

#### 2.1.2 Stopper Design and Parameterization

The stopper mechanism is a critical component for introducing controlled nonlinearity into the vibration energy harvesting system. Three iterative designs are developed to optimize structural integrity, contact behavior, and manufacturability, each addressing specific mechanical constraints identified through experimental and simulation analysis. All designs are modeled in SolidWorks® and parameterized for stiffness characterization.

Design Iteration 1: Bolted Rectangular Stopper with Semi-Cylindrical Tip



Figure 2.2. Stopper version 1

Mounting Interface: To maintain compatibility with the existing test rig configuration—where the cantilever beam is clamped between two thick plates secured by bolted connection—the stopper base is designed with four bolt holes. This allowed direct mounting onto the upper and lower surfaces of the clamping plates. The stopper base contour is precisely matched to the plate profile to ensure full-surface contact and eliminate mounting-induced stress.

Contact Geometry: Initial contact geometry utilized a square protrusion. However, finite element analysis revealed potential multi-point contact instability during beam impact. To enforce deterministic single-point contact, the interface is redesigned with a semi-cylindrical profile, converting the contact mode from surface-to-surface to line contact.

Structural Layout: A monolithic rectangular block (width = 100 mm, matching the clamping plates) with an integrated semi-cylindrical tip extending toward the beam. The oversized width relative to the beam (30 mm) provided torsional stability but incurred material redundancy.

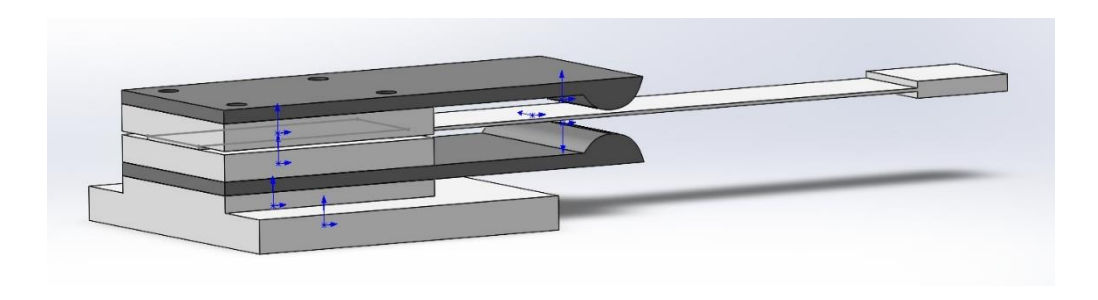


Figure 2.3. Assembly version 1

#### Design Iteration 2: L-Shaped Stopper Integrated Clamp



Figure 2.4. Stopper version 2

Mounting Revolution: Eliminating the separate clamping plates, this design integrated the clamping function directly into the stopper body. An L-shaped geometry is employed, where the horizontal leg bolted to the baseplate (two bolts D=13mm), and the vertical leg constrained the beam.

Stress Concentration Mitigation: A 10 mm fillet radius is added at the internal L-junction (Fig. 2.4) to reduce stress concentrations under impact loading. In this version, we keep the contact geometry constant.

Structural Layout: Compared with the first version of the stopper, this L-shaped stopper reduces the use of materials, increases support and optimizes the structure. It can clamp the beam directly, but there may be a problem of insufficient force to clamp the beam.

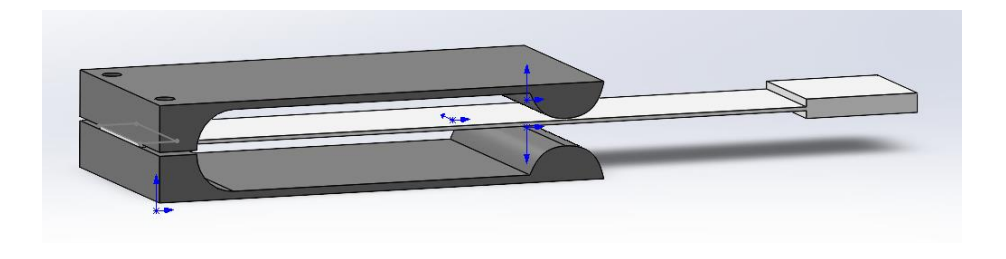


Figure 2.5. Assembly version 2

Design Iteration 3: T-Shaped Stopper with Beam-Matched Width

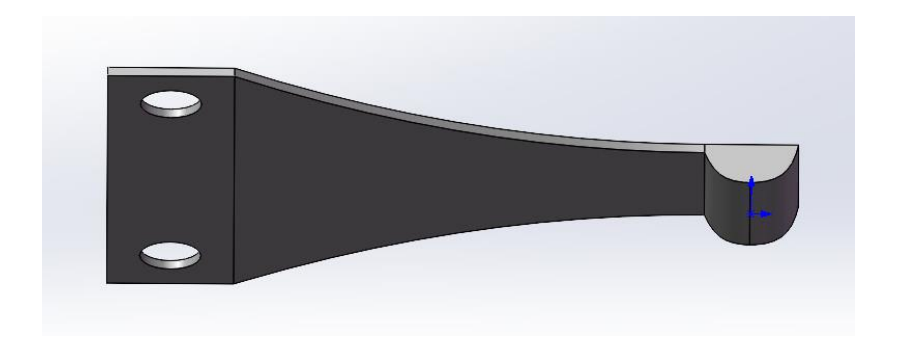


Figure 2.6. Stopper version 3

The final design evolution synthesizes the robustness of Version 1's plate-mounted interface with Version 2's space-efficient topology through a T-shaped structure which shows in figure 2.6, material reduction while effectively addressing stress concentration concerns and maintaining precise gap control.

In the mounting interface, the clamping plate integration is reintroduced to ensure rigid fixation of the cantilever beam. This configuration incorporates two Ø13 mm clearance holes for bolted connections, with optimized thickness dimensions which can be changed to adjust the gap between the beam and stopper contact surface while keep the thickness of connecting part of stopper constant.

For the contact region, the semi-cylindrical profile is retained while the width is reduced to match the beam width, resulting in material savings. Stress analysis shows concentration area at both transition regions of the T-junction, it's necessary to add structural reinforcements within these critical corners. The reinforcement geometry utilizes dual large-radius arc profiles precisely matching the stopper's effective length, maximizing structural integrity during impact loading scenarios.

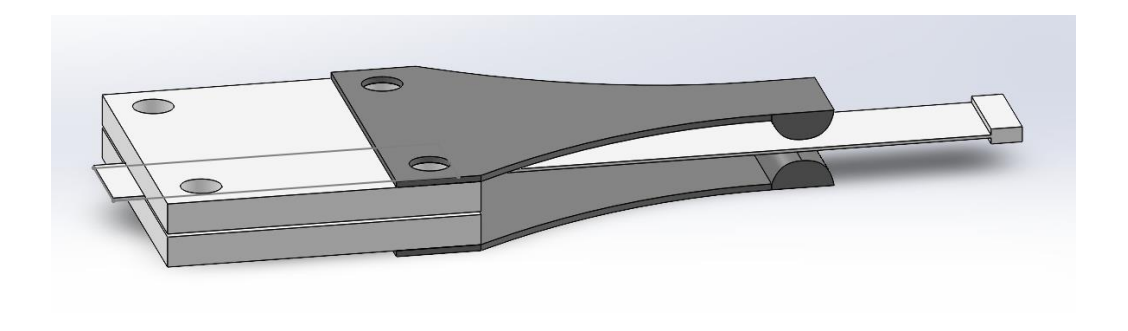


Figure 2.7. Assembly version 3

#### 2.2 Mathematical Model

#### 2.2.1 Modelling of the Linear System (with Piezoelectric Coupling)

The fundamental dynamics of the piezoelectric energy harvesting system are governed by a single-degree-of-freedom (SDOF) mass-spring-damper model coupled with a resistor-capacitor (RC) circuit. Under base excitation b(t), the governing equations are (1,2):

$$\begin{cases} m\ddot{z} + c_{v}\dot{z} + kz + \theta v = -m\ddot{b} \\ \frac{v}{R} + C_{p}\dot{v} = \theta\dot{z} \\ z = x - b \end{cases}$$

where

- z(t) = x(t) b(t): the displacement of the tip mass relative to the base excitation b(t),
- v(t): Piezoelectric output voltage
- $\theta$ : Electro-mechanical coupling coefficient, unit N/V.
- $m, c_v, k$ : Equivalent mass, viscous damping coefficient, linear stiffness of the beam

The second equation represents the electrical behavior of the piezoelectric element, which can be modelled as a current source in parallel with a capacitance  $C_p$ . The current generated by the piezoelectric layer is proportional to the strain rate (or equivalently, to  $\dot{z}$ ) through the electromechanical coupling coefficient  $\theta$ . This coefficient quantifies the bidirectional conversion between mechanical and electrical domains—specifically, the mechanical force generated per unit voltage or, equivalently, the electrical charge induced per unit displacement rate. Its SI unit is N/V, consistent with the term  $\theta v$  appearing as an equivalent restoring force in the mechanical equation.

In the context of the present study,  $\theta$  also determines how efficiently mechanical vibrations are converted into electrical energy and vice versa. As experimentally identified in Chapter 4, the average value of  $\theta$  is approximately 0.11 N/mV, while the intrinsic capacitance of the piezoelectric element is about 14.7 nF. These experimentally derived parameters validate the physical assumptions adopted in this theoretical model and are later used for quantitative comparison between simulations and measurements.

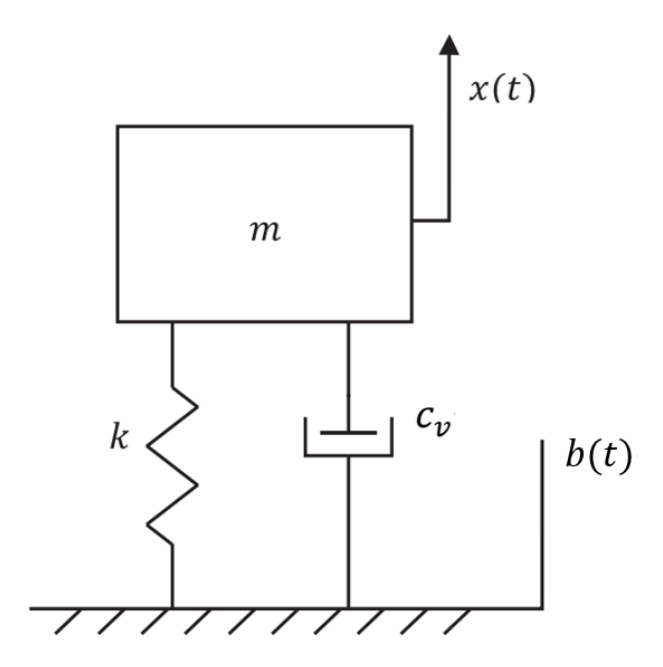


Figure 2.8: mathematical model of a single degree of freedom system with base excitations.

This model is valid only in the linear vibration regime where the cantilever does not contact the stoppers.

#### 2.2.2 Nonlinear Stopper Model

The physics of stopper nonlinearity originates from: when the tip displacement z is within the gaps  $g_{\pm}$ , the system behaves as a linear beam; once  $z > g_{+}$  or  $z < g_{-}$ , beam-stopper contact induces instantaneous stiffness surge.

The introduction of mechanical stoppers induces strong nonlinearity. The initial piecewise-linear restoring force model is

$$f_{nl}(z) = \begin{cases} k_s(z-g_+) & \text{If } z > g_+ \\ \phi & \text{If } g_- \le z \le g_+ \\ k_s(z+g_-) & \text{If } z < g_- \end{cases}$$

Arranged the nonlinear for function fNL:

$$\begin{cases} fNL\{1\} = k_s \times (z - g_+) \\ fNL\{2\} = -k_s \times (z + g_-) \end{cases}$$

where

-  $g_+/g_-$ : gaps between stoppers and beam surface

-  $k_s$ : equivalent stoppers stiffness

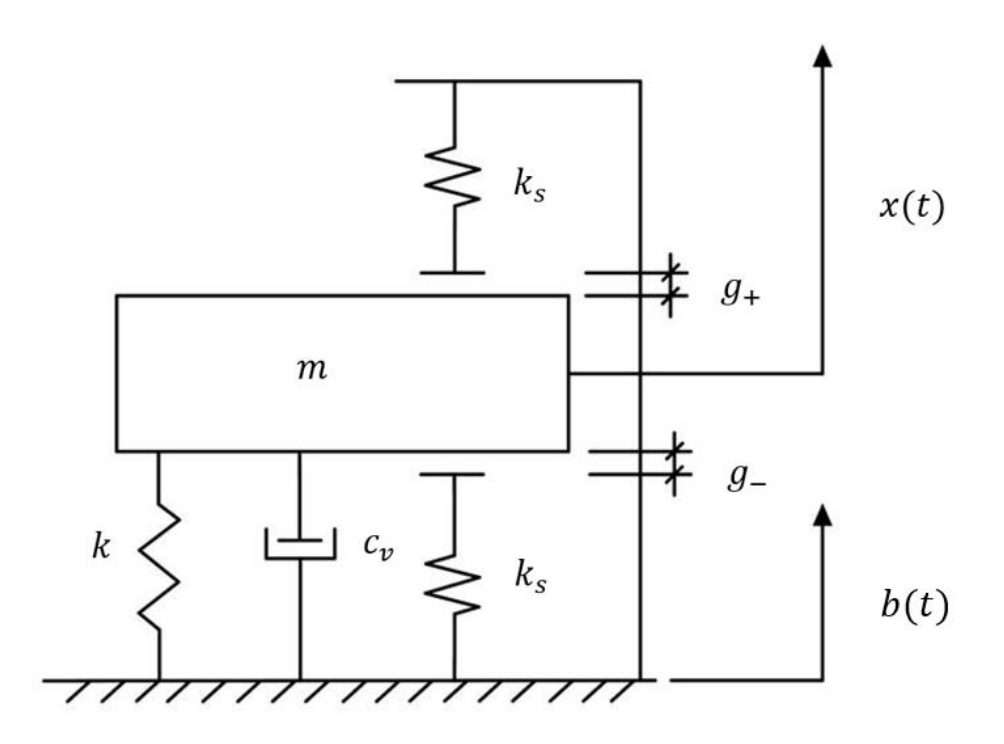


Figure 2.9. mathematical model of a single degree of freedom system with stoppers

Although capable of qualitatively capturing stiffness jumps and bandwidth enhancement, this model suffers from critical flaws: discontinuities in the restoring force and its derivative (equivalent stiffness) at contact points  $z = g_{\pm}$  cause convergence failure, computational instability, and accuracy degradation in numerical solvers (particularly for continuity-based integrators like the State Space method).

To address these issues, a piecewise smoothing technique is introduced. It constructs a smooth transition within an  $\varepsilon$ -neighborhood of the contact points:

$$rFun(x,\varepsilon) = \begin{cases} \frac{x-\varepsilon}{2\varepsilon} & \text{If } x > \varepsilon \\ \frac{1}{2\varepsilon} (x-\varepsilon)^2 & \text{If } 0 \le x \le \varepsilon \\ 0 & \text{If } x < \varepsilon \end{cases}$$

Where  $\varepsilon = 1 \times 10^{-5} [m]$  for negligible error

Reformed restoring force:

$$f_{nl}(z) = k_s[rFun(z - g_+, \varepsilon) - rFun(z + g_-, \varepsilon)]$$

Rectified the nonlinear force function  $f_{nl}$ :

$$\begin{cases} f_{nl}\{1\} = k_s * rFun(z - g_+, \varepsilon) \\ \\ f_{nl}\{2\} = -k_s * rFun(z + g_-, \varepsilon) \end{cases}$$

#### 2.2.3 Complete Nonlinear System Equations

The complete nonlinear system integrates piezoelectric coupling with smoothed stopper model:

$$\begin{cases} m\ddot{z}+c_v\dot{z}+kz+f_{nl}(z)+\theta v=-m\ddot{b}\\ \\ \frac{v}{R}+C_p\dot{v}=\theta\dot{z} \end{cases}$$

where

- $m, c_v, k$ : equivalent mass, viscous damping coefficient, linear stiffness of the beam
- $f_{nl}(z)$ : Nonlinear restoring force from mechanical stoppers (N)

This model captures three operational regimes:

- Linear regime  $(g_- \le z \le g_+)$ : Piezoelectric coupling dominant
- Transition regime ( $|z \pm g_{\pm}| < \varepsilon$ ): Smooth force transition
- Contact regime  $(|z| > g_{\pm} + \varepsilon)$ : Full stopper stiffness engaged

#### 2.3 Numerical Solution Method

The numerical solution strategy evolved from the State Space Method to the Newmark Integrator, addressing discontinuity issues induced by mechanical stoppers.

#### 2.3.1 Initial Approach: State Space Method

The state space method transforms the piezoelectric energy harvesting system into a set of first-order differential equations and describes the system evolution through state variables:

$$\{\dot{x}\} = [A]\{x\} + [B]\{u\}$$

where:

State Vector 
$$\{x\} = \begin{bmatrix} z \\ \dot{z} \\ v \end{bmatrix}$$
 Input Vector  $\{u\} = \begin{bmatrix} -m\ddot{y} \\ f_{nl}\{1\} \\ f_{nl}\{2\} \end{bmatrix}$ 

Nonlinear Function 
$$\begin{cases} f_{nl}\{1\} = k_s \times (z - g_+) \\ f_{nl}\{2\} = -k_s \times (z + g_-) \end{cases}$$

Dynamic Matrix 
$$[A] = \begin{bmatrix} 0 & 1 & 0 \\ -k/m & -c_v/m & -\theta/m \\ 0 & \theta/c_p & -1/(R \times c_p) \end{bmatrix}$$

Input Gain matrix 
$$[B] = \begin{bmatrix} 0 & 0 & 0 \\ 1/m & k_s/m & k_s/m \\ 0 & 0 & 0 \end{bmatrix}$$

#### 2.3.2 Enhanced Solution: Newmark Integrator

The Newmark- $\beta$  method is an implicit numerical integration scheme widely used for solving nonlinear structural dynamics equations. Its core concept discretizes continuous differential equations into stepwise algebraic equations via time domain decomposition. The method is built on two fundamental update equations:

$$\begin{cases} u_{t+\Delta t} = u_t + \dot{u}_t \Delta t + \left[ \left( \frac{1}{2} - \beta \right) \ddot{u}_t + \beta \ddot{u}_{t+\Delta t} \right] \Delta t^2 \\ u_{t+\Delta t} = \dot{u}_t + \left[ (1 - \gamma) \ddot{u}_t + \gamma \ddot{u}_{t+\Delta t} \right] \Delta t \end{cases}$$

where  $\beta = 0.25$  and  $\gamma = 0.5$  correspond to the unconditionally stable Constant Average Acceleration Method.

In this formulation, u represents the output vector  $\{z(t); v(t)\}$ . The Newmark method then utilizes z,  $\dot{z}$ , and  $\ddot{z}$  to solve the coupled equations for time-domain response analysis.

For nonlinear systems:

$$[M]\{\ddot{u}\} + [C]\{\dot{u}\} + [K]\{u\} + f_{nl}(u,\dot{u}) = \{F_{ext}(t)\}$$

Each timestep requires iterative solution:

- 1. Prediction: Estimate displacement/velocity using previous acceleration
- 2. Iteration: Compute nonlinear force residual, update acceleration
- 3. Convergence Check: Repeat until ||R|| < tol,  $tol = 1 \times 10^{-6}$

where ||R|| is the absolute residual on displacements and velocities.

In the study system, which is 2 degrees of freedom, there are one mechanical equation and one electrical equation:

$$\begin{cases} m\ddot{z} + c_v\dot{z} + kz + f_{nl}(z) + \theta v = -m\ddot{y} \\ \\ \frac{v}{R} + C_p\dot{v} = \theta\dot{z} \end{cases}$$

To use the Newmark- $\beta$  method (a numerical integration method for second-order differential equations), we need to transform the electrical equation into second-order form. Here is a trick: introduce a very small mass term (1 × 10<sup>-6</sup>  $\ddot{v}$ ) to turn the electrical equation into second order.

$$1\times 10^{-6}\ddot{v} + RC_p\dot{v} - R\theta\dot{z} + v = 0$$

In this way, the entire system can be written as a second-order differential equation in matrix form:

$$\begin{bmatrix} m & 0 \\ 0 & 10^{-6} \end{bmatrix} \begin{Bmatrix} \ddot{z} \\ \ddot{v} \end{Bmatrix} + \begin{bmatrix} c_v & 0 \\ -\theta R & RC_n \end{bmatrix} \begin{Bmatrix} \dot{z} \\ \dot{v} \end{Bmatrix} + \begin{bmatrix} k & \theta \\ 0 & 1 \end{bmatrix} \begin{Bmatrix} z \\ v \end{Bmatrix} + \begin{bmatrix} f_{nl}(z) \\ 0 \end{bmatrix} = \begin{bmatrix} -m\ddot{y} \\ 0 \end{bmatrix}$$

Where

- Mass Matrix [M]: m is a mechanical mass,  $1 \times 10^{-6}$  is a dummy electrical mass
- Damping Matrix [C]: Combines the mechanical damping  $c_v$  and the electrical damping term of piezoelectric coupling  $RC_p$  term
- Stiffness Matrix [K]: Integrates mechanical stiffness k and electro-mechanical coupling coefficient  $\theta$
- External Force  $\{F_{ext}(t)\}$ : Only mechanical excitation.

In the numerical solution process, the nonlinear forces induced by the stoppers are integrated into the system equations via a mapping mechanism. The nonlinear force function  $f_{nl}$  is decomposed into two independent components: the upper stopper force  $f_{nl}\{1\}$  and the lower stopper force  $f_{nl}\{2\}$ , each defined by a smoothed function of displacement:

$$\begin{cases} f_{nl}\{1\} = k_s * rFun(z - g_+, \varepsilon) \\ \\ f_{nl}\{2\} = -k_s * rFun(z + g_-, \varepsilon) \end{cases}$$

where rFun() is a piecewise quadratic smoothing function and  $\varepsilon$  is the smoothing width. The total nonlinear force is:

$$f_{nl}(z) = f_{nl}\{1\} + f_{nl}\{2\}$$

Through mapping vectors  $m\{1\} = [1,0]^T$  and  $m\{2\} = [1,0]^T$ , the scalar nonlinear forces are projected onto the system degrees of freedom to form the nonlinear force vector:

$$f_{nl} = m\{1\} f_{nl}\{1\} + m\{2\} f_{nl}\{2\} = \begin{bmatrix} f_{nl}(z) \\ 0 \end{bmatrix}$$

This vector acts solely on the mechanical degree of freedom (displacement z), while no nonlinear force is applied to the electrical degree of freedom (voltage v). During the iterative solution, the nonlinear force vector is updated in real-time based on the current displacement prediction, ensuring accurate capture of contact dynamics.

## 2.4 Model Objectives

The mathematical model aims to three aspects:

Firstly, characterize system dynamics. Quantify the mechanical and electromechanical behavior of the cantilever system:

- Without piezoelectric coupling: Analyze nonlinear stiffness effects induced by stoppers.
- With piezoelectric coupling: Evaluate voltage/power output under stochastic and harmonic excitations.

Secondly, optimize stopper parameters for maximum efficiency. Identify the best-performing stopper configuration by:

- Determining optimal stiffness  $k_s$  and gap distances  $g_+$  and  $g_-$  that maximize piezoelectric efficiency (power density per unit excitation).
- Balancing bandwidth expansion against power amplification across operational scenarios.

Finally, correlate parameters with physical design rules. Establish quantitative relationships between:

- Optimized parameters  $k_s$ ,  $g_{\pm}$  and physical properties (stopper material, geometry, assembly tolerance).
- Nonlinear dynamics (e.g., contact force, stiffness switching) and harvester performance metrics (e.g., RMS power, bandwidth gain).

## 3. Numerical Simulation

#### 3.1 Introduction

This chapter details the numerical simulations conducted to analyze the models developed in the Modelling section. All models are implemented and solved within the MATLAB script.

Prior to verifying the MATLAB code models, a stiffness analysis of the stopper components is performed. This analysis uses SolidWorks simulation study to determine displacement data under load, which is incorporated into the MATLAB code to calculate the stopper stiffness.

The MATLAB simulation process begins with an analysis of the linear system to establish its baseline characteristics to provide a reference for subsequent nonlinear analysis. Following the modelling sequence, the state-space method is initially attempted to directly integrate the piecewise functions to simulate the nonlinear system. However, convergence issues occurred due to discontinuities at the transition points. To deal with this, a piecewise smoothing technique is applied to the nonlinear functions. Subsequently, the Newmark-Beta method is used for time-domain integration to optimize the integration method. Finally, simulations are performed under varying base excitation amplitudes to compare the responses of both the linear and nonlinear systems.

## 3.2 Stopper Stiffness Estimation

The stiffness analysis of the stoppers is primarily conducted using Static Study functionality in SolidWorks. In the static study, appropriate boundary conditions are applied into the stopper model which means the stoppers are fixed at an end through the clamping plate and then apply a static load at the designated contact area. The resulting displacement at the contact point is probed and used to calculate stiffness  $(k_s = F / x_displacement)$ .

This analysis is performed by varying the effective length and thickness of the stopper designs to determine their influence on stiffness.

#### 3.2.1 Material Properties and Boundary Conditions

The stopper material is defined as Polylactic Acid (PLA) to reflect the properties of the 3D-printed components intended for subsequent experimental validation. PLA is selected based on its economic viability for printing multiple design variations and its suitability, as the modelling phase focuses on optimizing the stopper geometry for both material efficiency and structural integrity. The key PLA material parameters used in the simulation are summarized in Table 3.1.

Property	Value	Units
Elastic Modulus	3500000000	$N/m^2$
Poisson's Ratio	0.35	N/A

Shear Modulus	2400000000	$N/m^2$
Mass Density	1250	$kg/m^3$
Tensile Strength	50000000	$N/m^2$
Compressive Strength	17926368.97	$N/m^2$
Yield Strength	60000000	$N/m^2$
Thermal Conductivity	0.13	$W/(m \cdot K)$
Specific Heat	1800	$J/(kg \cdot K)$

Table 3.1. PLA Material Properties

Following material assignment, the boundary conditions for the study are established. Based on the stopper's mounting method, applying two Fixed Geometry fixtures to the surfaces of the two mounting holes and the base surface in contact with the clamping plate, as shown in Figure 3.1.

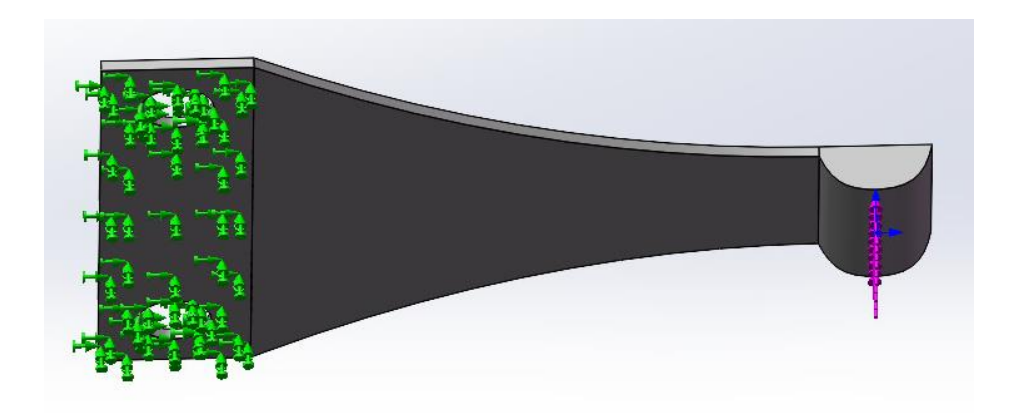


Figure 3.1. T-Shaped Stopper Boundary Conditions and External Load

To simulate the maximum force the stopper might experience in experiment, a static load is applied at the contact point. Although the stopper would typically experience impact loads in practice, applying the maximum anticipated static force represents a worst-case scenario for stiffness estimation. For directly calculating stiffness of stopper via equation  $k_s = F / \delta_s$  a nominal static force 1N is applied. The displacement is obtained by reading the results in the contact point.

#### 3.2.2 Stiffness estimation

As discussed above, stopper stiffness values are derived from SolidWorks® finite element analysis (FEA) under static loading conditions. The FEA assumed perfectly rigid boundary conditions at the mounting holes and linear elastic behavior of the PLA material. Under these assumptions, the stoppers are treated as purely elastic elements with no dynamic contribution of their own.

The general results indicated that stopper stiffness is approximately  $ks \approx 2.5 \times kb$  where kb is the equivalent stiffness of the cantilever beam. These estimated values are subsequently implemented in the MATLAB numerical model. It must be emphasized, however, that at this stage no experimental calibration is available; thus, the results should be regarded as theoretical predictions based on idealized conditions.

In the stopper design process, several geometrical variations are considered by adjusting thickness and effective length, since these parameters strongly influence stiffness. The design objective is to select a stopper stiffer than the beam itself, thereby ensuring engagement sufficient to induce the expected hardening effect, but not so rigid as to behave like a rigid wall that would entirely suppress beam motion.

After considering both mechanical performance and practical manufacturability via 3D printing, a design with 2 mm thickness and 90 mm effective length is selected as a balance between structural efficiency and material economy. The SolidWorks static study predicted a displacement of  $1.729 \times 10^{-3} m$  under a nominal applied load of 1 N, corresponding to a stiffness of:

$$ks = F / \delta \approx 578.37 N/m$$

This value is slightly higher than the equivalent stiffness of the cantilever beam, which is considered optimal for generating hardening-type nonlinearities without fully constraining the system motion. The chosen stiffness therefore represents a suitable compromise, allowing the stopper to act as an effective nonlinear limiter for bandwidth expansion. Once established, this stiffness parameter is directly implemented in the MATLAB numerical model to evaluate the dynamic response under nonlinear conditions.

### 3.3 Linear System Benchmark Validation

The linear benchmark simulation serves to validate the fundamental electromechanical model before introducing nonlinearities. This step is essential to ensure that the equivalent mass–spring–damper representation of the cantilever and the piezoelectric coupling are correctly implemented.

#### 3.3.1 Natural Frequency and Damping Validation

The natural frequency of the equivalent SDOF beam model is calculated based on beam geometry and material properties using:

$$k = \frac{3EI}{l^3}$$
 ,  $m = m_{tip} + \frac{1}{3}m_{beam}$ 

resulting in an estimated frequency  $f_N = \frac{1}{2\pi} \sqrt{\frac{k}{m}} = 10.514 \ Hz$  .

The computed value is compared against the measured natural frequency from experimental modal testing ( $f_N = 10.5 \, Hz$ ). The discrepancy is found to be within acceptable limits (error < 0.1332%), confirming that the simplified SDOF approximation reasonably captures the system's dynamics.

The damping ratio is taken from experimental measurements ( $\zeta_m = 0.7\%$ ) and implemented as viscous damping. This parameter ensures that numerical predictions reflect realistic decay behavior near resonance.

The restoring force—displacement and potential energy functions are also plotted, confirming the expected linear elastic behavior. These plots provide a baseline reference for subsequent comparisons with the nonlinear stopper system, where the restoring force deviates from linearity.

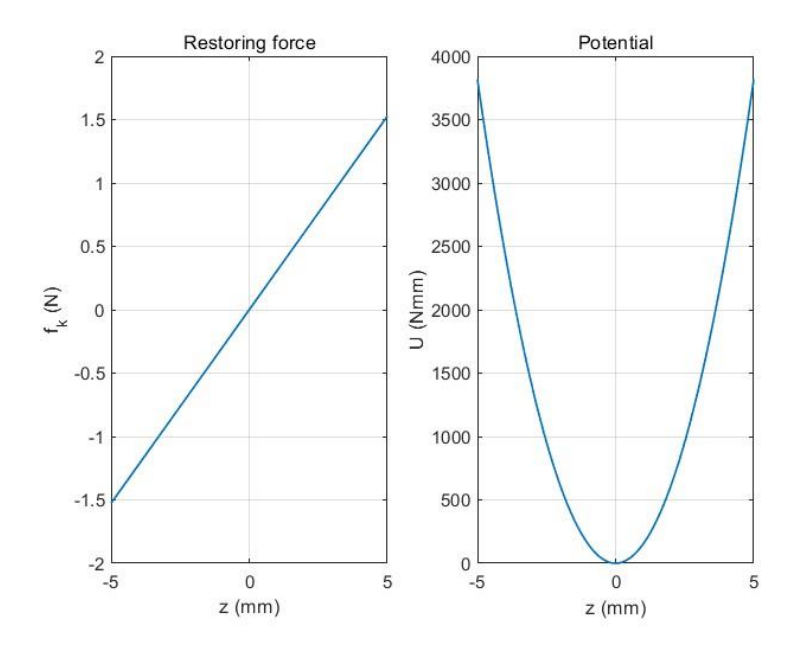


Figure 3.2 – Restoring force–displacement relation (left) and potential energy function (right) of the equivalent linear SDOF cantilever beam. These plots confirm the expected linear elastic behavior and provide the baseline reference for later nonlinear comparison.

#### 3.3.2 Frequency Response of the Linear System under Harmonic Excitation

Harmonic base excitation is applied to the linear system, and analytical transfer functions are used to compute the frequency response. Both structural transmissibility and voltage output are examined:

- Transmissibility curves: The transfer function  $G_{zb} = |Z_0/B_0|$  which, represents the output displacement (relative) compared to the input one, is calculated with and without piezoelectric coupling. Results confirmed the expected resonance amplification at the natural frequency, along with damping-induced bandwidth limitations. The inclusion of piezoelectric coupling slightly altered the transmissibility curve, reflecting the electromechanical interaction between mechanical energy and electrical energy. (see Figure 3.3 top left)
- Voltage response: The transfer function  $|G_{vb} = V_0/B_0|$  represents the voltage output per unit base displacement. A clear resonance peak is observed near 10.5 Hz, consistent with theoretical predictions. Similarly, the transfer function  $G_{vz} = |V_0/Z_0|$  describes the electromechanical sensitivity to beam relative (see Figure 3.3 top right and 3.4).
- Phase response: The phase of both structural and voltage outputs displayed the characteristic second-order system behavior, with a  $\pi/2$  shift around resonance. This confirmed that the implemented damping model correctly captured the dynamic lag between input excitation and system response.

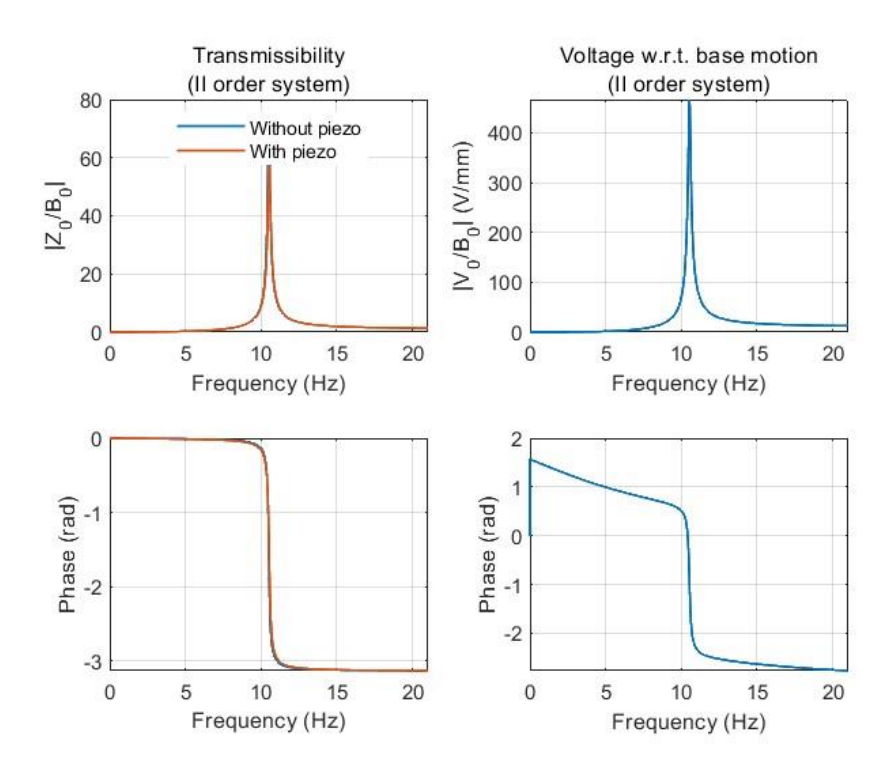


Figure 3.3 – Frequency response of the linear piezoelectric cantilever under harmonic base excitation. Top row: magnitude of transmissibility (left) and voltage output per unit base displacement (right). Bottom row: corresponding phase responses. The characteristic  $\pi/2$  phase shift at resonance is evident, confirming the second-order system behavior.

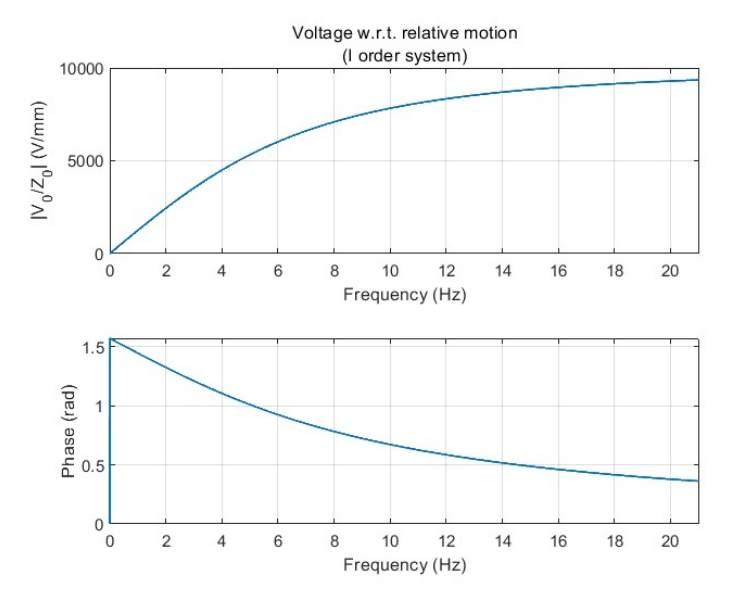


Figure 3.4 – Voltage response relative to the beam's relative displacement.

The magnitude (top) shows the electromechanical sensitivity of the piezoelectric disk.

The phase response (bottom) highlights the dynamic lag between mechanical deformation and electrical output.

Overall, the benchmark simulations demonstrate that the linear piezoelectric cantilever model is correctly implemented and provides reliable predictions. These results serve as a reference baseline against which the nonlinear stopper system can later be evaluated, highlighting deviations introduced by piecewise stiffness and impact dynamics.

#### 3.4 State-Space Method: Discontinuity-Induced Divergence

As introduced in Section 2.3.1, the state-space method provides a compact mathematical framework for representing the coupled electromechanical system in first-order form. While Chapter 2 outlined the theoretical formulation of this method, the present section focuses on its application to the nonlinear piezoelectric beam with mechanical stoppers. In particular, frequency sweep simulations are performed in order to evaluate whether the method could capture the expected nonlinear phenomena, namely resonance hardening and bandwidth broadening.

#### **Motivation and Expected Outcomes**

The objective of this stage is to exploit the state-space formulation to investigate the nonlinear response of the system under sweep excitation. Two specific outcomes are targeted:

- Hardening behavior, manifested as a resonance peak shift to higher frequencies compared with the linear system.
- Bandwidth broadening, observable in the voltage response and harvested power, which would demonstrate improved robustness of the harvester under variable excitations.

If successfully captured, these effects would confirm the beneficial role of mechanical stoppers in enhancing vibration energy harvesting performance.

#### Simulation and Representative Result

The system is excited with a linear frequency sweep ranging from  $0.9f_N$  to  $1.5f_N$ , with base displacement amplitude of 0.5 mm. Nonlinear restoring forces from the stoppers are incorporated into the formulation as displacement-dependent input terms, while the state-space matrices remained constant.

A representative outcome is shown in Figure 3.5, which illustrates the restoring force decomposition into linear and nonlinear components. The nonlinear term becomes active once the displacement exceeds the stopper gap, thereby modifying the overall restoring force characteristic. This confirms that the state-space model formally accounts for the presence of the stopper nonlinearity.

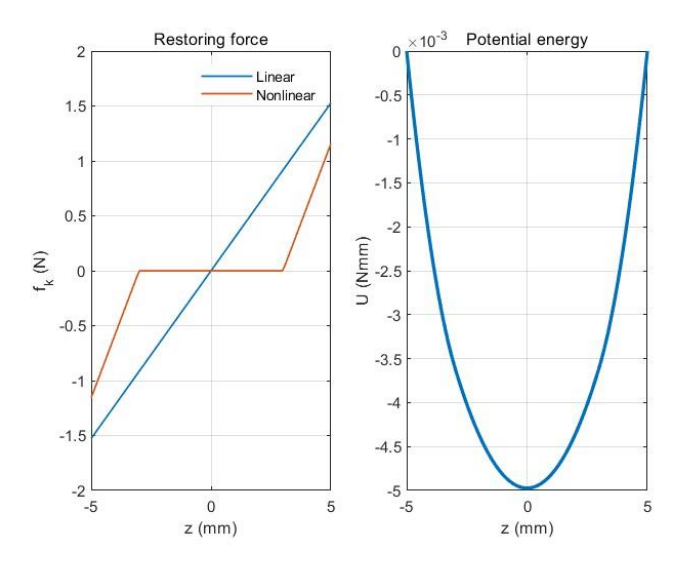


Figure 3.5: Restoring force decomposition with linear and nonlinear contributions.

Although the formulation is successful in embedding the nonlinear restoring force, the actual dynamic responses obtained under frequency sweep excitation did not reveal the expected phenomena. Specifically:

The transmissibility curves produced by the state-space simulations closely resembled those of the linear system, without a clear rightward shift of the resonance peak.

The voltage output spectra also failed to demonstrate consistent bandwidth broadening.

Time-domain responses showed contact events, but these did not translate into significant nonlinear signatures in the frequency domain.

Due to these issues, additional figures such as frequency response functions, voltage time histories, and spectral analyses are not presented here. They are found to be nearly indistinguishable from the linear benchmark and thus provided no meaningful insight into the nonlinear behavior. For clarity, only the restoring force representation is reported as evidence of the attempted formulation.

In summary, the state-space method is tested as an initial numerical strategy for simulating the nonlinear piezoelectric system. While it demonstrated the ability to formally include nonlinear restoring forces, it failed to reproduce the essential nonlinear features of interest, namely resonance hardening and bandwidth broadening. The main limitations arose from the assumption of constant system matrices and the difficulty of handling discontinuous contact dynamics within the state-space framework.

For these reasons, the study transitioned to the Newmark-β integration method (Section 3.4.2), which is more robust for directly solving second-order nonlinear differential equations with discontinuous restoring forces.

## 3.5 Newmark-\( \beta \) Method: Implementation and Convergence Analysis

Following the limitations observed with the state-space formulation, where discontinuous nonlinearities associated with the stoppers induced divergence and prevented stable solutions, the analysis is advanced using the Newmark- $\beta$  method. This direct time-domain integration scheme provided the stability and flexibility required to incorporate the piecewise nonlinear restoring forces of the stopper mechanism, while maintaining numerical convergence across a wide range of operating conditions.

In contrast to the state-space model, the Newmark formulation allowed the system to be studied under more realistic excitation scenarios, including both harmonic sweeps and broadband random inputs. This flexibility is essential to capture the nonlinear dynamics of the system and to evaluate how different configurations of stopper stiffness  $k_s$  influence harvesting efficiency. The chosen parameters ( $\beta = 0.25$ ,  $\gamma = 0.5$ ) ensured stability, while a pseudo-mass term is added to the electrical equation to unify the governing equations into a second-order system. To ensure smooth transitions across the contact boundaries, the piecewise nonlinear force is regularized using a quadratic smoothing function, which reduced numerical instabilities while retaining the essential hardening characteristics of the system.

#### 3.5.1 Stiffness Optimization after Experimental Limitations

During the initial testing of the 3D-printed stopper designs, it became evident that the system did not achieve the expected hardening effect. Instead of broadening the frequency response, the stopper behavior is closer to a rigid constraint, limiting the dynamic range of the cantilever beam. This shortcoming motivated a redesign in the numerical domain, where the excitation is shifted from the vertical test setup to a lateral excitation model. Within this revised framework, the role of the stopper stiffness  $k_s$  became central: rather than focusing on a single design, a systematic optimization is performed to identify a feasible range of stiffness values capable of inducing the desired nonlinear response.

The optimization is carried out numerically by enumerating a series of stiffness values. Starting from the stiffness derived from SolidWorks simulations (approximately  $5.78 \times 10^2 \ N/m$ ), the range is progressively extended up to  $5 \times 10^3 \ N/m$ . For each candidate stiffness, the Newmark integration produced voltage and displacement responses, from which two performance metrics are extracted: the voltage per unit base displacement ( $V/mm\ RMS$ ) and the average electrical power ( $W\ RMS$ ).

By comparing these results across successive sets of simulations, the optimal stiffness window is identified not as a single value but as a narrow range, approximately between 2600 and 2680 N/m. Within this interval, both normalized voltage and harvested power achieved their peak values, confirming the suitability of moderately stiff stoppers to enhance system bandwidth

without inducing rigid constraints.

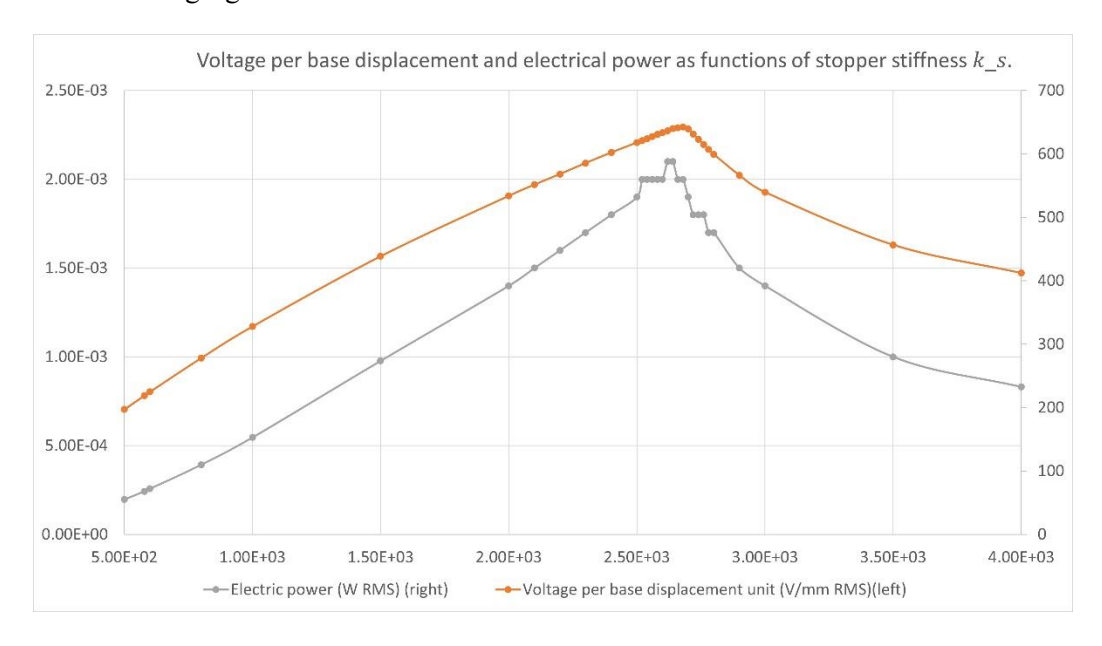


Figure 3.6: Voltage per base displacement and electrical power as functions of stopper stiffness  $k_s$ . The shaded region highlights the identified optimal stiffness window.

Although the numerical analysis identified an approximate optimal stiffness range, it is important to recognize that the actual stiffness of the fabricated stoppers inevitably differs from the idealized numerical values. For this reason, the stiffness range should be regarded primarily as a reference rather than a strict design target. Different stiffness values may lead to distinct system behaviors, and understanding this spectrum of responses is as relevant as locating the peak-performing configuration. The selected interval therefore provides guidance for design but does not replace the need for broader evaluation across feasible stiffness values.

#### 3.5.2 Random Excitation and Broadband Validation

Building upon the stiffness optimization study in Section 3.5.1, the response of the system under random base excitation is further investigated to evaluate the effectiveness of the nonlinear stoppers in broadband energy harvesting. This step is particularly significant because most real-world vibration sources—such as wind, traffic, or machinery—are inherently stochastic rather than purely harmonic. Validating performance under random excitation therefore provides a more realistic assessment of the system's applicability for practical energy harvesting.

To this end, simulations are conducted for both the linear and nonlinear configurations while progressively increasing the base excitation amplitude,  $B_0$ . For each case, the root-mean-square (RMS) voltage normalized by the base displacement,  $\eta = V_{RMS}/V_0$ , and the RMS electrical power,  $P_e$ , are calculated. The comparison is shown in Figure 3.7 and Figure 3.8.

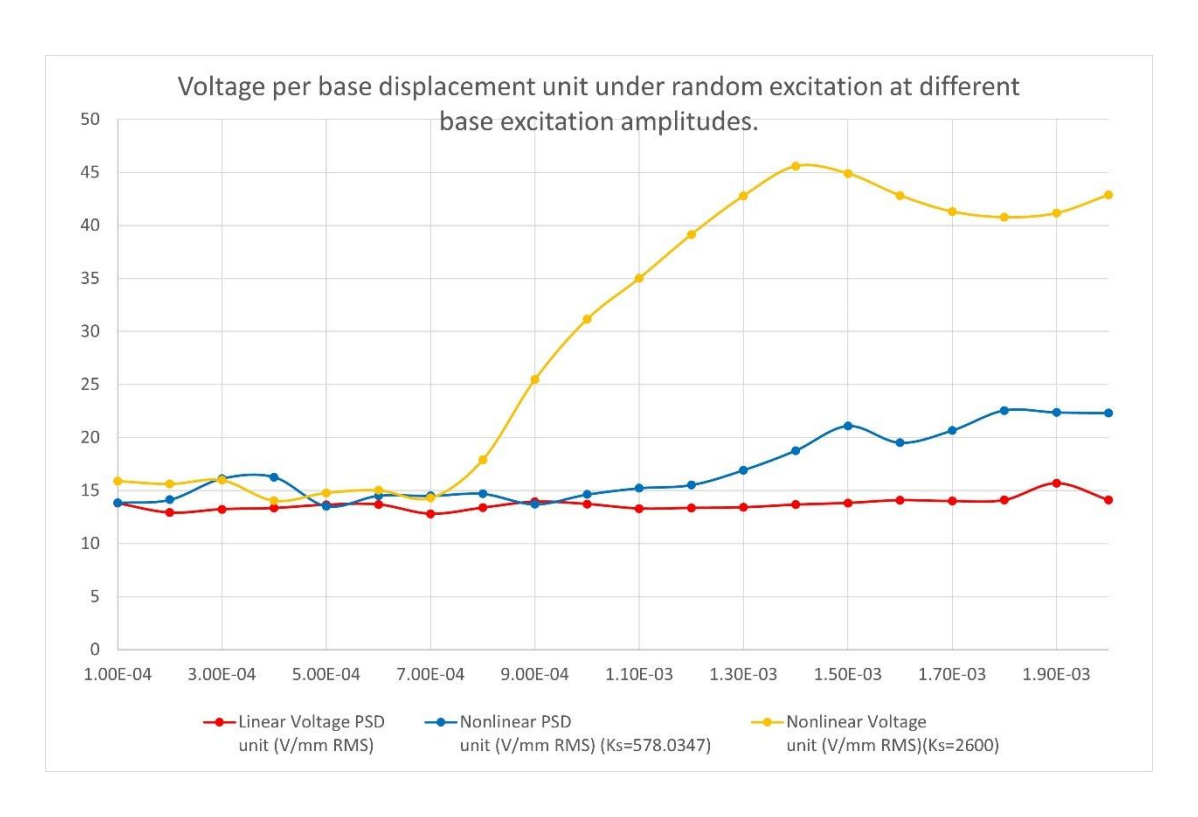


Figure 3.7: Voltage per base displacement unit under random excitation at different base excitation amplitudes. (Linear  $k_s = 0 N/m$ ,  $k_s = 578 N/m$ ,  $k_s = 2600 N/m$ )

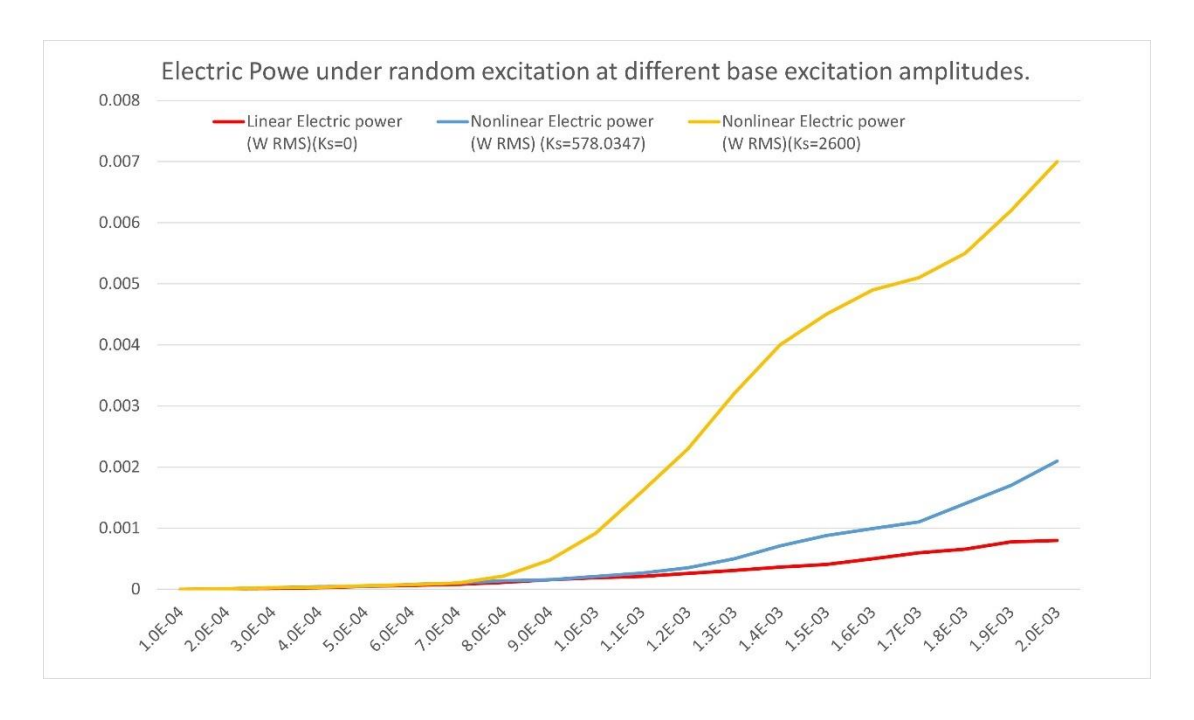


Figure 3.8: Electrical power vs. excitation amplitude for linear and nonlinear cases.

For the linear case, both  $\eta$  and  $P_e$  scale nearly proportionally with excitation amplitude, reflecting the narrowband and resonance-limited nature of the system. In contrast, the nonlinear cases exhibit a much steeper increase, with curves that progressively diverge from the linear baseline as  $B_0$  grows. Notably, when the stopper stiffness is optimized to  $k_s = 2600 \, N/m$ , the nonlinear performance advantage is further amplified, yielding significantly higher efficiency at larger excitation amplitudes. These results highlight not only the fundamental role of nonlinear stoppers in enhancing energy capture under stochastic conditions, but also the sensitivity of the outcome to stopper design parameters.

#### 3.5.3 Numerical Outputs and Convergence Considerations

While the random excitation analysis highlights the superior performance of the nonlinear harvester under broadband environmental inputs, these observations remain primarily at the level of global performance indices such as voltage-per-displacement and harvested power. To gain a deeper understanding of the underlying mechanisms, it is essential to complement these results with a spectral analysis. By examining the frequency-domain outputs of the Newmark- \$\beta\$ simulations, one can directly observe how nonlinear stoppers redistribute vibrational energy and alter the cumulative power characteristics compared with the linear configuration. This transition from random-input validation to frequency-domain evaluation also provides an opportunity to address the convergence limitations encountered with the state-space method and to confirm the robustness of the Newmark scheme in strongly nonlinear regimes.

The Newmark- $\beta$  simulations yield a series of outputs that provide critical insights into the performance of nonlinear harvesters. Among these, the most important indicators are the voltage power spectral density (PSD) and the cumulative electrical power spectrum, both of which highlight the redistribution of vibrational energy under nonlinear dynamics.

For the linear configuration, the PSD exhibits a sharp and symmetric resonance peak centered at  $\approx 10.5~Hz$ , with a maximum amplitude of  $30.85~V^2/Hz$  at 10.53~Hz (Figure 3.9). This narrowband behavior reflects the inherent limitation of linear harvesters, which can only operate efficiently when environmental vibrations coincide with the natural frequency of the cantilever. Correspondingly, the cumulative electrical power rises steeply around the resonance and then gradually levels off, reaching  $\approx 1.11 \times 10^{-5}~W$  at 11~Hz and continuing a slow increase until  $\approx 1.27 \times 10^{-5}~W$  at 30~Hz (Figure 3.10). The gradual saturation of the cumulative curve underscores that the energy contribution outside resonance is negligible in the linear case.

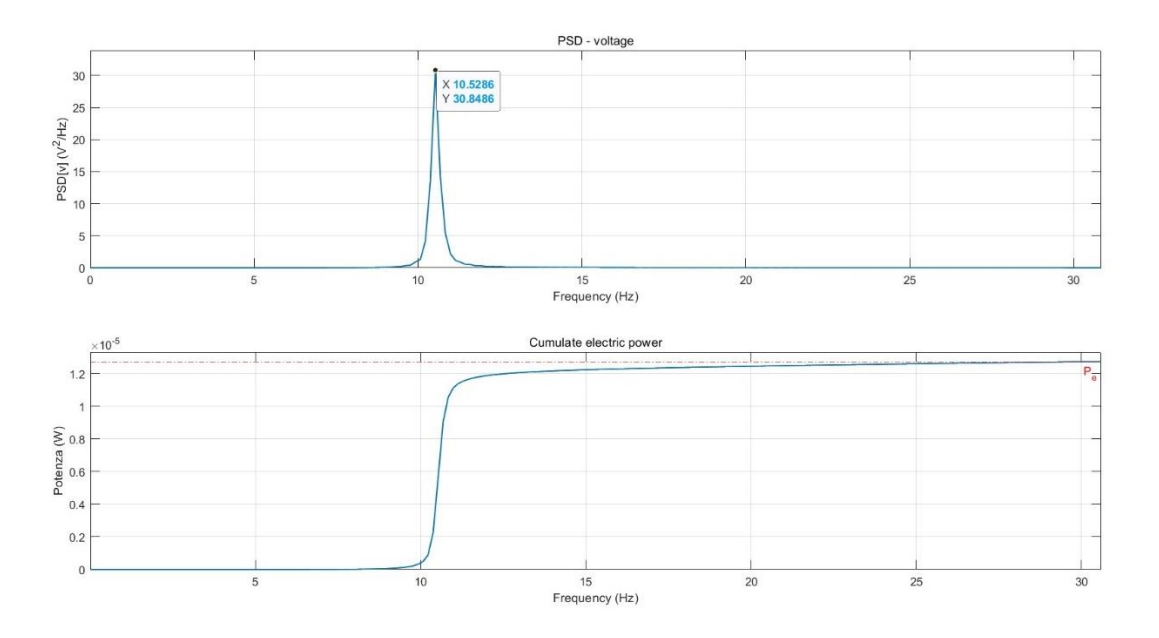


Figure 3.9: Voltage power spectral density (PSD) of the linear configuration, showing a symmetric peak at  $10.5 \, Hz$  (30.85  $V^2/Hz$ ).

Figure 3.10: Cumulative electrical power of the linear configuration, rising sharply at resonance and gradually saturating at  $\approx 1.27 \times 10^{-5} W$  by 30 Hz.

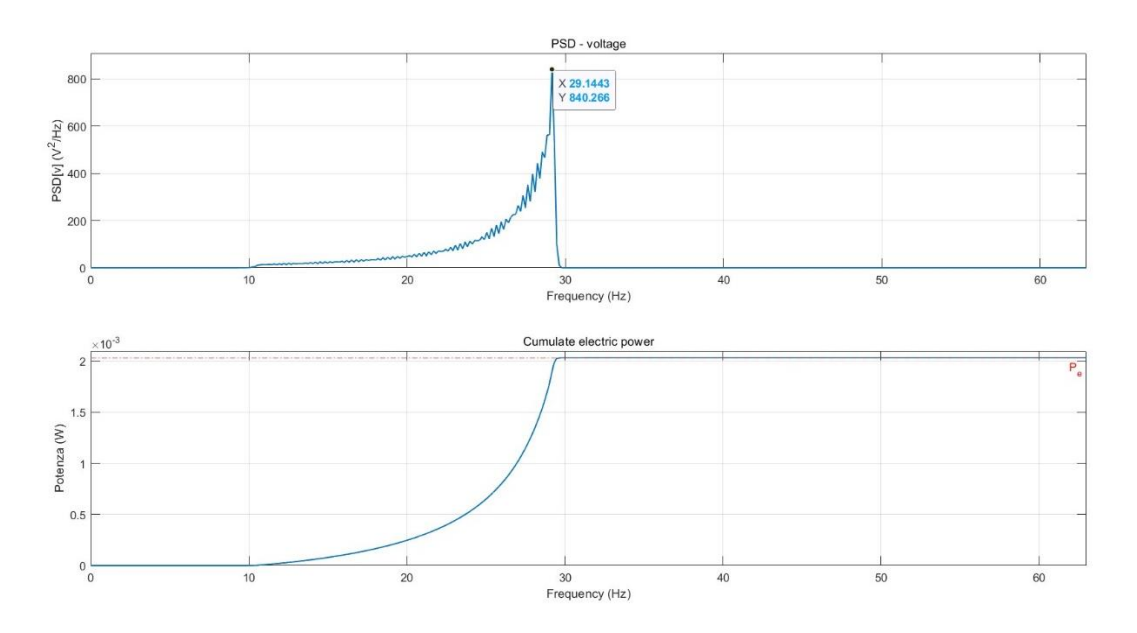


Figure 3.11: Voltage power spectral density (PSD) of the nonlinear configuration ( $ks \approx 2600 \ N/m$ ), rising with fluctuations to a sharp maximum of  $840.27 \ V^2/Hz$  at  $29.14 \ Hz$ , followed by a steep drop.

Figure 3.12: Cumulative electrical power of the nonlinear configuration, increasing nearly linearly with frequency and reaching  $\approx 0.002 \, W$  by 29.3 Hz.

By contrast, the nonlinear configuration with optimized stopper stiffness ( $ks \approx 2600 \, N/m$ ) produces a markedly different spectral signature. Instead of a symmetric peak, the nonlinear PSD rises progressively from the resonance frequency, forming a fluctuating curve that culminates in a sharp maximum of  $840.27 \, V^2/Hz$  at  $29.14 \, Hz$ . The subsequent steep drop suggests that nonlinear interactions effectively concentrate and then abruptly release spectral energy (Figure 3.11). This behavior is directly reflected in the cumulative power curve (Figure 3.12), which increases almost parabolically with frequency and reaches  $\approx 0.002 \, W$  by  $\approx 29.3 \, Hz$ . Unlike the linear system, where energy continues to accumulate gradually beyond the resonance, the nonlinear case demonstrates that the bulk of the harvested energy is accumulated rapidly within the low-frequency band, leaving little contribution at higher frequencies.

This comparison leads to an important conclusion: nonlinear stoppers do not merely broaden the frequency response by smearing out resonance but instead redistribute energy through successive off-resonance contributions, which build up until a sharp cutoff is reached. The cumulative power profile illustrates that nonlinear harvesters are able to capture energy more efficiently within a confined frequency band, transforming distributed excitations into concentrated electrical output. This mechanism explains why the nonlinear cumulative curve exhibits an almost monotonic rise up to the saturation point, as opposed to the more gradual and plateau-like trend of the linear case.

From a numerical perspective, these outputs further validate the robustness of the Newmark- $\beta$  integration scheme. Unlike the state-space approach discussed in §3.4, which often suffered divergence under strong nonlinearities, the implicit corrections in Newmark iterations ensured convergence across the tested stiffness values, including the highly nonlinear  $ks = 2600 \, N/m$  case. The ability to obtain stable PSD and power spectra under such conditions confirms that the solver captures nonlinear effects without introducing artificial instabilities. This convergence reliability lends strong confidence to the physical significance of the observed broadband redistribution and energy enhancement.

Beyond the spectral analysis, additional outputs from the Newmark- $\beta$  simulations provide further confirmation of the nonlinear effects. Figure 3.11-12 compared the PSD and cumulative power curves, illustrating how the nonlinear configuration redistributes vibrational energy over a broader range and accumulates nearly all of the harvested power below 30 Hz, in sharp contrast to the narrowband linear case. To complement these frequency-domain results, three further time- and input-domain perspectives are considered.

Figure 3.13-14 presents the decomposition of restoring forces into total, linear, and nonlinear contributions as functions of time and displacement. In the linear system, the restoring force is strictly proportional to displacement, yielding a single, symmetric trend without discontinuities. By contrast, the nonlinear system shows an additional force component that becomes active when the beam reaches the stopper gaps. This contribution modifies the restoring force profile,

producing asymmetric loops and an increased effective stiffness during large deflections. Such behavior confirms the intended hardening-like mechanism of the stoppers and provides a direct physical interpretation of the bandwidth broadening observed in the PSD analysis.

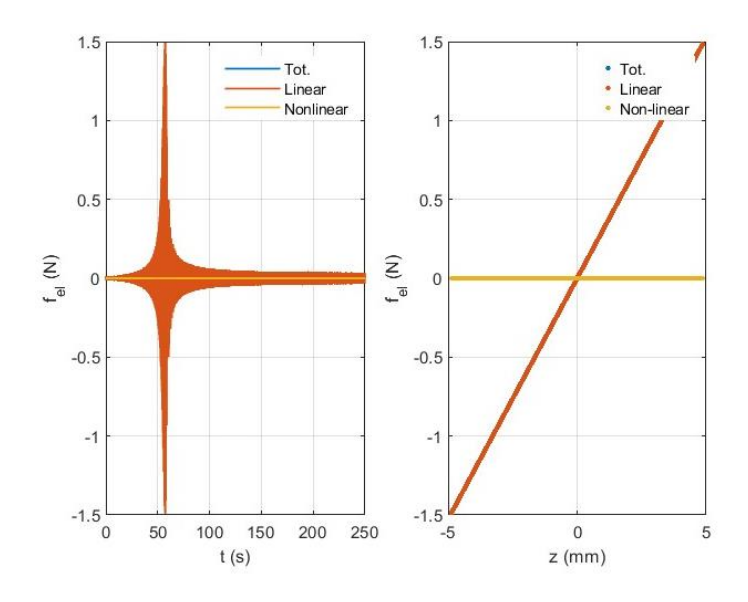


Figure 3.13 – Restoring force decomposition in linear system.

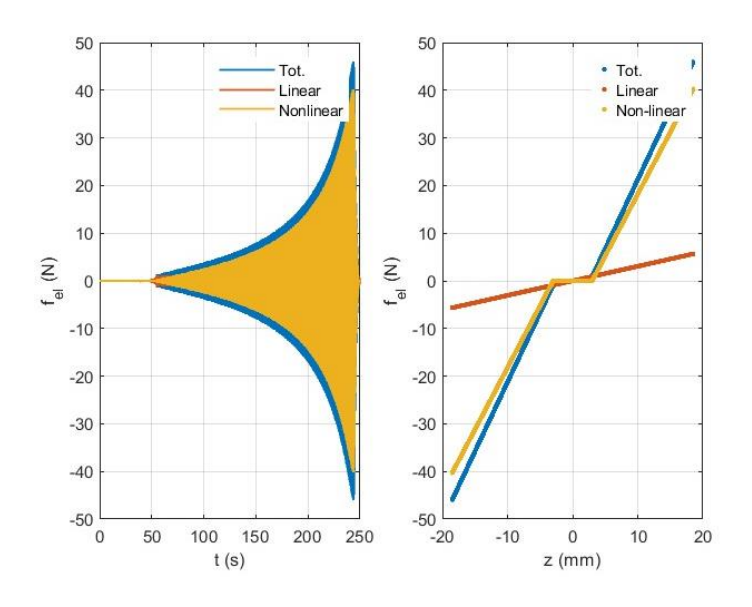


Figure 3.14 – Restoring force decomposition in nonlinear system: total, linear, and nonlinear contributions. (ks = 2600 N/m)

Figure 3.15-16 shows the voltage and displacement responses over time. In the linear system, the voltage output closely follows the harmonic nature of the base excitation, with a nearly sinusoidal waveform synchronized to displacement. For the nonlinear case, the response exhibits richer harmonic content and intermittent modulation, reflecting the interaction between

the beam and the stoppers. Despite these nonlinearities, the Newmark method ensures numerical stability, with the solutions converging to bounded, periodic responses rather than diverging as observed with the state-space method. This robustness underscores the method's suitability for analyzing strongly nonlinear harvesters.

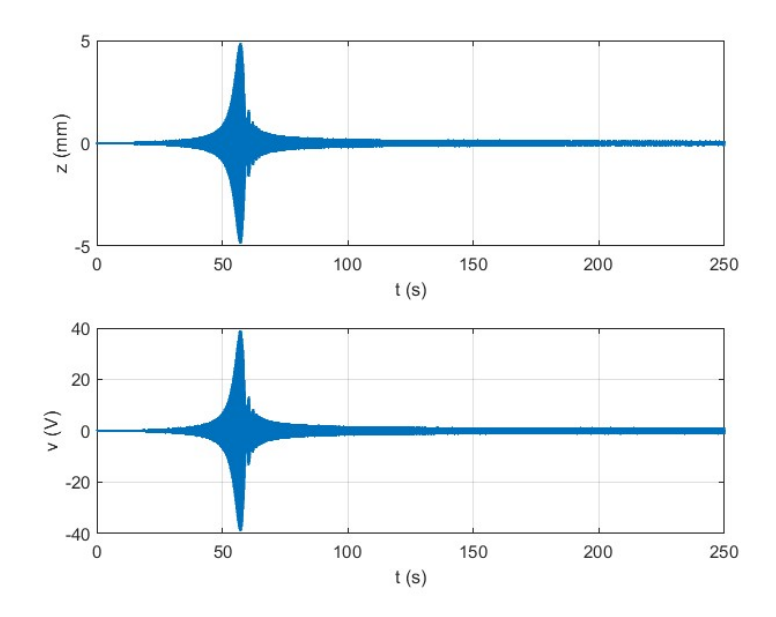
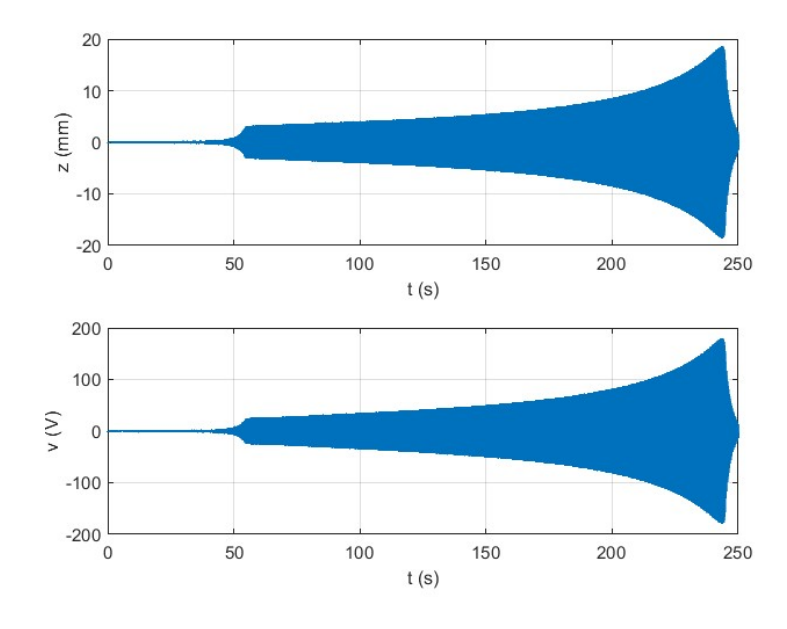


Figure 3.15 – Time histories of displacement and voltage for linear system.



 $Figure \ 3.16-Time \ histories \ of \ displacement \ and \ voltage \ for \ nonlinear \ system.$ 

$$(ks = 2600 N/m)$$

Finally, Figure 3.17-18 compares the ratio between the output voltage amplitude  $V_0$  and the input excitation amplitude  $Y_0$ . The linear configuration shows a monotonic but limited amplification near resonance, whereas the nonlinear system achieves significantly higher voltage gain across a wider input range. This confirms that nonlinearity not only broadens the frequency bandwidth but also enhances the effective transduction from mechanical input to electrical output.

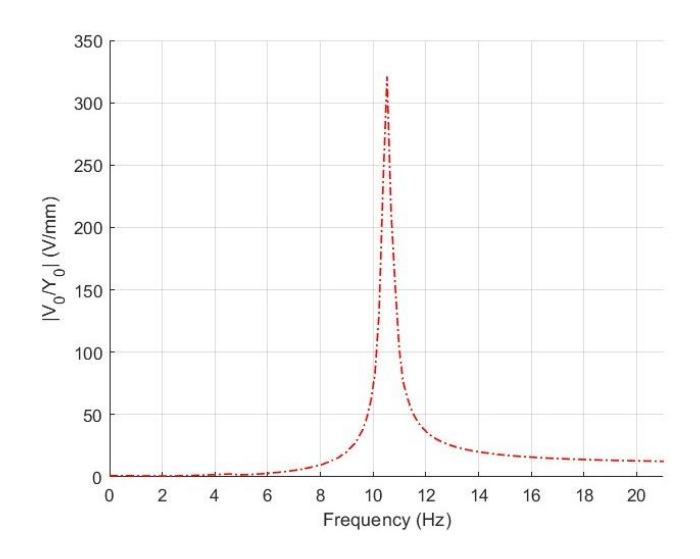


Figure 3.17 – Voltage-to-input ratio  $V_0/Y_0$  for linear system.

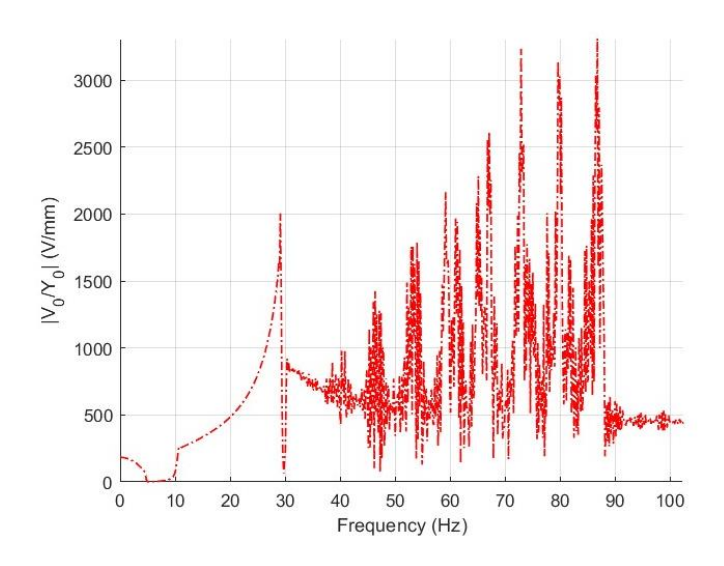


Figure 3.18 – Voltage-to-input ratio  $V_0/Y_0$  for nonlinear system.

Taken together, these outputs demonstrate that the nonlinear stoppers fundamentally alter the dynamics of the system. They extend the operational bandwidth, enable more efficient energy transfer at off-resonance frequencies, and maintain stable convergence under challenging conditions where the state-space approach fails. This validates the adoption of the Newmark- $\beta$  method as the principal numerical tool for analyzing nonlinear piezoelectric energy harvesters.

### 3.6 Error and Convergence Analysis

The numerical analysis carried out in this chapter revealed critical differences between the two implemented approaches: the state-space formulation and the Newmark-β integration method. The state-space approach, although mathematically elegant, failed to converge when applied to the nonlinear system with mechanical stoppers. This failure is primarily due to the intrinsic discontinuities introduced by contact events: when the beam displacement exceeded the stopper gap, the effective stiffness suddenly increased, producing sharp transitions in the restoring force. In the state-space framework, these discontinuities are embedded directly in the system matrices, causing the dynamic matrix to lose smoothness and leading to unstable numerical integration. As a result, the simulations often terminated without producing meaningful frequency sweep outputs, or generated responses nearly indistinguishable from the linear case, thereby preventing the extraction of reliable nonlinear characteristics.

By contrast, the Newmark- $\beta$  method demonstrated a robust capability to handle nonlinearities, even under strong contact interactions. This stability arises from the implicit time-integration scheme, which evaluates displacement and velocity predictions iteratively within each time step, thereby allowing the nonlinear restoring forces to be consistently updated until convergence is achieved. As shown in the previous sections, the method successfully captured nonlinear features such as the broadening of the operational bandwidth, the redistribution of spectral energy in the PSD, and the amplification of voltage and power under random excitation. Importantly, convergence is maintained even when the stopper stiffness is varied over a wide range, and numerical instabilities could be controlled by adjusting the time step size.

The comparison between the two methods highlights a key methodological insight: while the state-space formulation is effective for linear piezoelectric models, it is not well-suited for discontinuous nonlinearities, where abrupt stiffness transitions dominate the dynamics. The Newmark- $\beta$  method, on the other hand, offers a general and reliable tool for nonlinear vibration energy harvesting analysis, capable of providing stable and physically consistent outputs across different excitation scenarios. This justifies its adoption as the main numerical approach for the nonlinear simulations presented in this thesis.

# 4. Experimental Tests

Following the numerical analysis presented in Chapter 3, a series of experimental investigations are conducted to verify the model predictions and to explore the system behavior under increasing levels of mechanical nonlinearity. The experiments are performed on the same cantilever beam described in Chapter 2, equipped with a piezoelectric patch and a tip mass, and mounted on an electrodynamic shaker capable of generating controlled base excitations.

Initially, the beam response is characterized under purely linear conditions, without any mechanical constraint, to validate the stiffness, damping, and electromechanical parameters identified through the numerical simulations. Subsequently, a nonlinear configuration is tested by introducing a pair of 3D-printed beam shaped stoppers designed to limit the beam's vibration amplitude. However, as will be discussed later, the flexibility of the printed material and the vertical testing configuration introduced additional dynamic interactions not foreseen by the model. This observation led to a later redesign of the stopper geometry and test orientation, which are presented in the following sections of this chapter.

### 4.1 Linear Experimental Setup and Measurement System

The experimental rig consisted of a clamped–free steel beam instrumented with accelerometers and a bonded piezoelectric patch. The beam is mounted vertically on a rigid base plate connected to an electrodynamic shaker. The shaker provided controllable base excitation, while a 1 M $\Omega$  resistive load is used to measure the generated electrical voltage. The tip of the beam carried an added mass of 56.3 g to reproduce the same dynamic properties used in numerical simulations. The setup is shown in Figure 4.1.

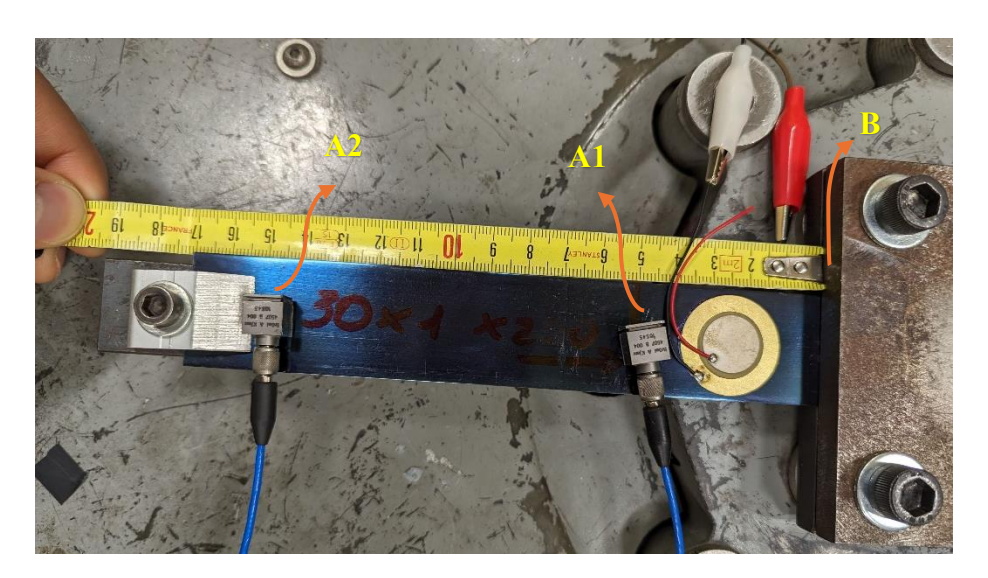


Figure 4.1. Linear experimental setup showing the beam, shaker, and sensors.

The linear configuration served as the fundamental validation step for both the mechanical and electromechanical aspects of the model. The beam is excited harmonically and randomly across a frequency range of 3–50 Hz, and acceleration and voltage responses are acquired simultaneously. The recorded signals are processed in MATLAB using the *pwelch* and *tfestimate* functions to compute the power spectral densities (PSDs), transmissibilities, and transfer functions between the base excitation and the beam response.

In the time domain, the base acceleration and the beam responses exhibit clean oscillations, with consistent phase and amplitude ratios among the measured signals, confirming the structural integrity of the setup and the absence of nonlinearities. The piezoelectric voltage follows the same trend, maintaining linear proportionality with the beam deformation. These results are presented in Figure 4.2, where the waveforms demonstrate that the beam operates stably in its first bending mode and behaves as a single-degree-of-freedom (SDOF) system.

In the frequency domain, the power spectral densities (PSDs) of the accelerations and the piezoelectric voltage all exhibit a pronounced resonance peak centered at approximately 10.5 Hz, as shown in Figure 4.3. This frequency coincides precisely with the numerically predicted first natural frequency reported in Chapter 3, validating the accuracy of the finite element model and the boundary conditions used therein. The sharp and symmetric resonance peak confirms that the system's response remains strictly linear, with no evidence of stiffness or damping variations under the applied excitation levels.

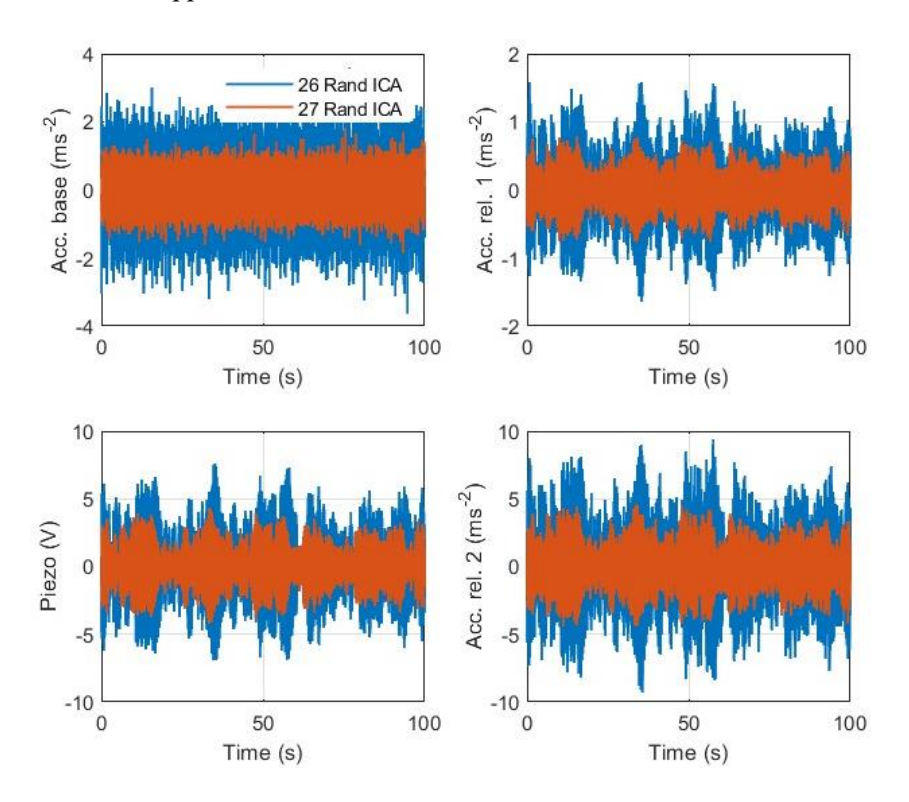


Figure 4.2 – Time-domain signals: base acceleration, relative accelerations at mid-span and tip, and piezoelectric voltage.

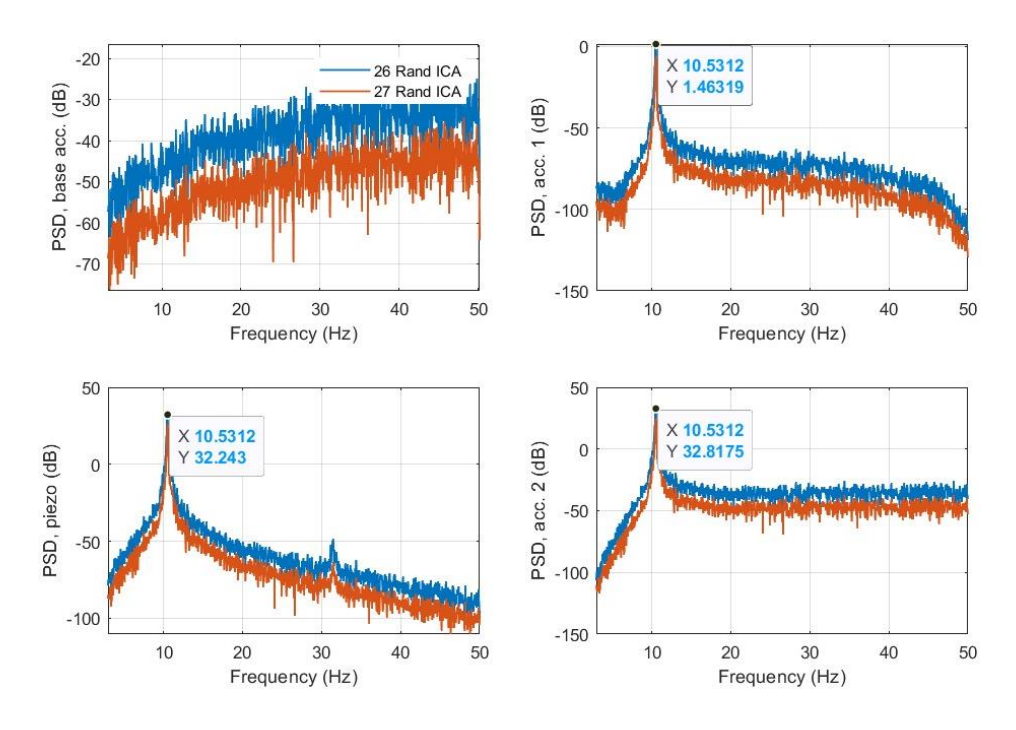


Figure 4.3 – Power spectral densities of base acceleration, beam tip acceleration, and piezoelectric voltage. A clear resonance peak appears at 10.5 Hz.

The frequency-response functions (FRFs) between the base and beam accelerations,  $G_{A1-B}(f)$  and  $G_{A2-B}(f)$ , together with the transfer function between base acceleration and piezoelectric voltage output,  $G_{vb}(f)$ , are plotted in Figures 4.4.

As described in Table 1 (Sensor Configuration) in *Section 2.1.1*, accelerometer A1 is positioned at mid-span of the beam to capture its intermediate dynamic response, A2 is mounted at the beam's free tip to measure the maximum deflection amplitude, and B is fixed at the base to record the input excitation. This configuration allows for a detailed comparison between local beam motions and the global base input, ensuring accurate characterization of both mechanical and electromechanical transfer functions.

All three magnitude curves show a distinct resonance at 10.5 Hz, and their corresponding phase plots reveal a  $-90^{\circ}$  crossing typical of a lightly damped second-order system. The close correspondence between the mechanical transfer functions  $G_{A2-B}(f)$  and the electromechanical function  $G_{vb}(f)$ , indicates that the piezoelectric output voltage is directly correlated to the beam's vibration amplitude, confirming the electromechanical coupling assumptions adopted in the numerical model.

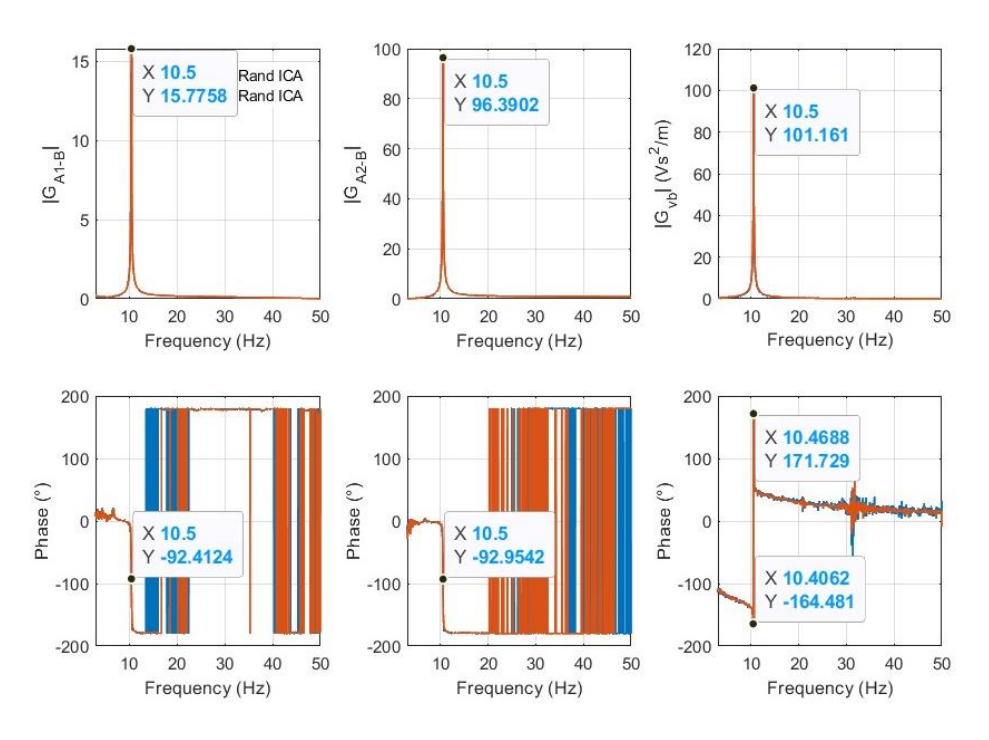


Figure 4.4 – Frequency-response functions of the beam and piezoelectric output. The magnitude and phase exhibit identical resonance behavior at 10.5 Hz.

The electromechanical transfer functions  $G_{v-z_2}(f)$  and  $G_{v-\dot{z}_2}(f)$ , shown in Figure 4.5, describe the voltage response of the piezoelectric patch as a function of the beam's local displacement and velocity at the tip.

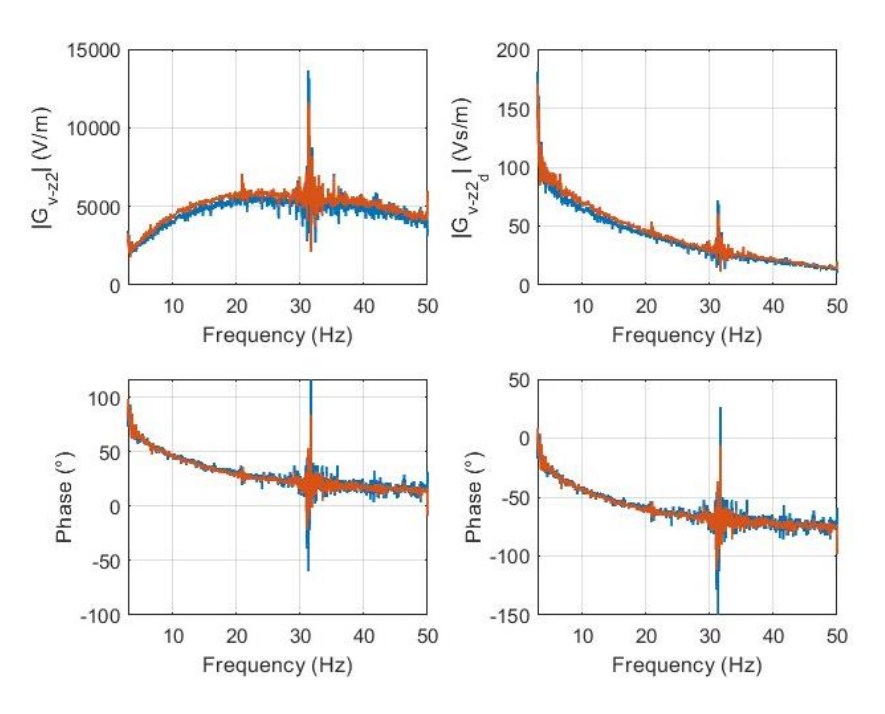


Figure 4.5 – Electromechanical transfer functions  $\,G_{v-z_2}(f)\,$  and  $\,G_{v-\dot{z}_2}(f)\,$ 

The measured magnitude curves exhibit a smooth decay with increasing frequency, without any pronounced resonance peak, as expected for a first-order electromechanical system. At lower frequencies, the voltage output follows the beam velocity proportionally, while at higher frequencies it approaches an almost constant value determined by the capacitive nature of the piezoelectric element and the resistive load. A small irregularity appears near 31 Hz, which can be attributed to higher-mode effects or experimental noise rather than an actual resonance.

Overall, the results confirm the validity of the linear electromechanical model introduced in Chapter 2, demonstrating that the piezoelectric transducer behaves consistently with the expected first order coupling dynamics. This provides a solid baseline for comparison with the nonlinear experiments discussed in the following sections.

### 4.2 First Nonlinear Experimental Setup and Measurement System

Following the validation of the linear behavior described in Section 4.1, a second experimental configuration was implemented to investigate the nonlinear dynamic response of the piezoelectric cantilever system. In this setup, a pair of 3D-printed beam-shaped stoppers was mounted symmetrically around the beam tip, as illustrated in Figure 4.6. These stoppers were designed to introduce contact during large-amplitude motion, reproducing the nonlinear stiffness characteristics previously discussed in the modelling phase.

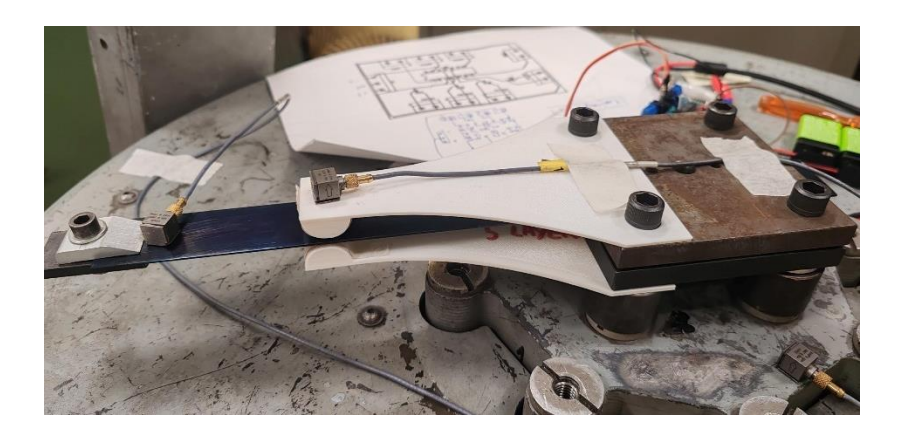


Figure 4.6: Experimental setup showing the beam, shaker, stopper mount, and sensors.

The purpose of this configuration was to experimentally verify the feasibility of the nonlinear contact mechanism and to assess the structural interaction between the beam and the stopper. A stopper geometry with a target stiffness of 578.37 N/m, as predicted by static finite-element simulation in SolidWorks, was adopted. This stiffness level was selected to introduce a moderate degree of nonlinearity without excessively constraining the beam's motion, allowing for measurable deformations under base excitation.

However, as later observed during testing, the actual stiffness of the printed resin material differed significantly from the nominal simulated value, resulting in unexpected dynamic interactions between the beam and the stopper. These discrepancies highlight the sensitivity of the system's nonlinear response to material compliance and manufacturing tolerances.

To better quantify this discrepancy, a prototype stopper was fabricated and experimentally tested to verify its actual stiffness characteristics. As shown in Figure 4.7

During preliminary tests, the actual stiffness of the printed resin material was found to be considerably lower than the predicted value, leading to unexpected dynamic interactions between the beam and the stopper. This deviation emphasizes the influence of material compliance and manufacturing tolerance on the system's nonlinear response, underlining the importance of accurately characterizing the real mechanical properties of the stoppers before further optimization.



Figure 4.7 — 3D-printed Beam-shaped stopper

The printed part exhibited a much higher flexibility than expected, mainly due to the anisotropic and layer-dependent mechanical properties inherent to FDM manufacturing. A subsequent static compression test on the printed stopper confirmed this deviation, revealing an effective stiffness of approximately 220 N/m — significantly lower than the predicted 578 N/m.

During the test, the stopper's compliance introduced several unexpected effects. Its low stiffness allowed noticeable deformation under dynamic loading, while gravitational effects further influenced its deflection, shifting the effective contact point with the cantilever beam. Moreover, due to its own flexibility, the stopper exhibited a resonant behavior close to the beam's first natural frequency, causing an undesired energy exchange between the two components. Consequently, the system failed to exhibit the expected hardening effect, which is predicted in the numerical analysis. These results indicate that although the initial concept successfully demonstrated the mechanical interaction between beam and stopper, the actual implementation could not reproduce the intended nonlinear stiffening behavior.

This preliminary attempt, however, is crucial in identifying the key limitations of the vertical setup. The excessive compliance of the printed stopper, combined with the influence of gravity, demonstrated that the vertical base excitation configuration is inherently unsuitable for achieving a stable and repeatable nonlinear contact condition.

Consequently, in the subsequent phase, the experimental system is redesigned to operate with a horizontal base excitation, effectively eliminating the gravitational bias on the stopper and contact region. The new configuration maintained the same cantilever beam, tip mass, and piezoelectric elements, but incorporated a semi-cylindrical stopper geometry specifically developed to provide higher stiffness and a more controlled nonlinear interaction.

The redesign and the optimization of this improved configuration are discussed in the following subsection.

#### 4.2.1 Stiffness Optimization and Redesigned Stopper

Following the limitations observed in the first nonlinear test, where the 3D-printed stoppers failed to induce the expected hardening effect, the experimental configuration is redesigned to obtain a controlled nonlinear response.

In this stage, the test setup is modified to eliminate gravitational influence and improve the mechanical consistency of contact between the beam and the stopper. A new semi-cylindrical stopper geometry is designed and implemented, allowing more uniform lateral contact and a stable response under harmonic and random base excitation.

The next section presents the rationale behind the redesign, the experimental configuration, and the theoretical framework adopted for evaluating the nonlinear behavior of the modified system.

### 4.3 Experimental Reconfiguration and Motivation

In the initial nonlinear setup, the vertical orientation introduced additional static loads due to gravity, which affected the dynamic equilibrium of the beam–stopper system. These loads caused asymmetric contact conditions and led to unstable resonance responses. Additionally, the printed stopper structure exhibited greater flexibility than expected, making it unable to produce the desired hardening effect. As a result, the experimental response remained nearly linear, and the nonlinear phenomena predicted numerically could not be validated.

To overcome these challenges, the test setup is completely reconfigured to operate under horizontal base excitation. In this arrangement, gravity no longer influenced the contact dynamics, allowing the beam to interact symmetrically with the stopper along its oscillation direction. A top-view schematic of this experimental configuration is presented in Figure 4.8. This configuration provided more reliable and repeatable results while maintaining the same beam—tip mass—piezoelectric assembly as in the previous linear analysis, ensuring that comparisons between linear and nonlinear behaviors remained meaningful.

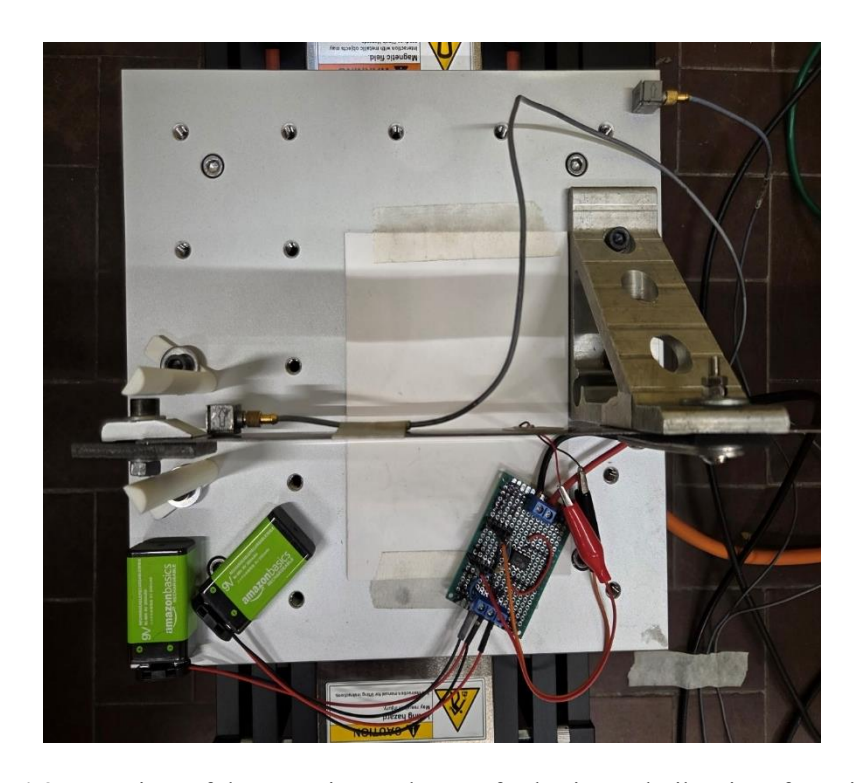


Figure 4.8: Top view of the experimental setup for horizontal vibration, featuring the cantilever beam, tip mass, and semi-cylindrical stopper.

An additional refinement is introduced in the installation and alignment of the stopper to address both geometric asymmetry and gap control. Because the mounting holes on the shaker table are not symmetrically positioned with respect to the beam, the beam could not be centered precisely between the available fixing points. At the same time, the originally designed 3 mm clearance between the beam and the stopper is found to be excessively large, allowing unwanted lateral motion and contact uncertainty. To minimize these effects, the gap is reduced to approximately 0.5–1 mm, and the stopper is relocated near the tip mass to act as a motion limiter with improved control of the contact region. A detailed close-up of this critical gap is provided in Figure 4.9.



Figure 4.9: Close-up view detailing the gap between the beam tip mass and the semicylindrical stopper.

To achieve the desired alignment under the asymmetric mounting constraints, the stopper is installed with an approximately 45° rotation relative to the beam axis. This orientation effectively compensated for the hole offset while maintaining the optimized small gap. As a result, the actual contact line between the beam and the semi-cylindrical stopper is rotated by about 45° with respect to the configuration used in the numerical stiffness estimation. Although this geometric modification slightly changed the local contact direction, it did not affect the global nonlinear behavior of the system or the validity of the experimental results. Instead, it simply required the effective stiffness range to be re-evaluated in the numerical model to account for the new contact geometry, thereby maintaining consistency between experimental and simulated interpretations.

#### 4.3.1 Design Concept of the Semi-Cylindrical Stopper

The newly designed semi-cylindrical stopper evolved directly from the original beam-aligned configuration. In the first design, the stopper and the beam are arranged in parallel, and the contact occurred along a narrow line defined by a small rounded edge at the stopper's tip. This configuration ensured a well-defined contact interface but is highly sensitive to deformation, especially under vertical loading. In the redesigned horizontal system, the same concept of line contact is maintained, but the rounded contact section is extended longitudinally, forming a semi-cylindrical surface that runs along the beam's vibration direction. This geometry provided both smoother contact interaction and an improved stiffness distribution along the stopper's length.

The semi-cylindrical stopper functions as a motion limiter, governing the maximum allowable deflection of the beam and inducing the desired nonlinear hardening effect once contact occurs. The stopper's base is reinforced with a flat positioning plane, allowing it to be firmly fixed to the horizontal shaker table. The design incorporated elongated mounting holes, enabling small but precise adjustments of the gap distance, now refined to 0.5–1 mm. This modification reduced unwanted free motion and enhanced the repeatability of the contact events across multiple tests.

Moreover, the transition from vertical to horizontal excitation required a new mechanical arrangement of the stopper's base. The elongated semi-cylindrical tip is supported by a short rectangular base plate, ensuring structural stability and allowing for the necessary torque resistance during vibration. To further strengthen the connection between the semi-cylindrical body and its mounting plane, a filleted triangular reinforcement is added, effectively redistributing stress concentrations observed in preliminary simulations. This ensured that the stopper retained its shape and stiffness properties throughout repeated impacts during the nonlinear tests.

The complete 3D CAD model of the redesigned stopper is presented in Figure 4.10, showing the semi-cylindrical contact region, mounting plane, and elongated holes for adjustable alignment. Finite element analysis of this model estimated its stiffness to be approximately 3261.58 N/m, a value derived by applying a 1 N static force at the contact point with the tip mass and calculating the resulting displacement. The physically realized stopper component, fabricated using PLA material, is shown in Figure 4.11. These refinements collectively ensure that the mechanical design is robust enough to maintain stable contact behavior while preserving the targeted nonlinear characteristics essential for validating the numerical predictions.

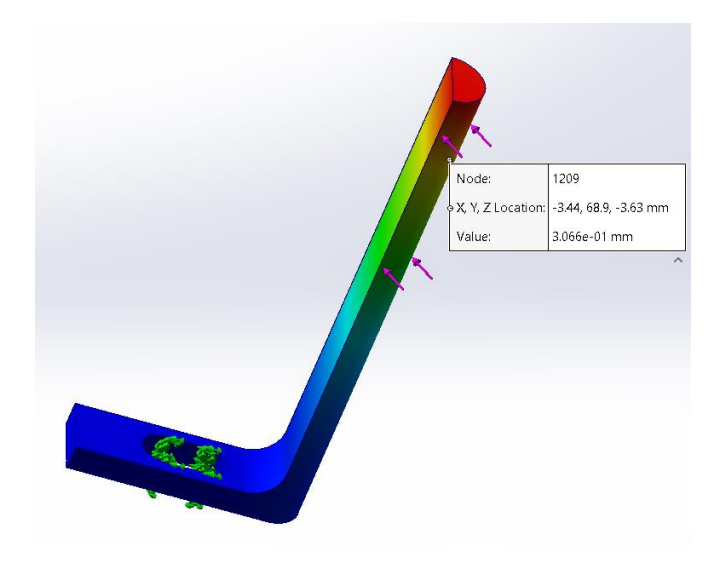


Figure 4.10: 3D CAD model and static simulation of the semi-cylindrical stopper.

The design features a semi-cylindrical contact region and a mounting plane with alignment constraints. The displacement field resulting from a 1 N static force applied at the 45° contact interface is shown, indicating the deformation used for stiffness estimation.



Figure 4.11: Physically realized stopper component fabricated using PLA material.

### 4.4 Nonlinear Experimental Validation

With the reconfigured setup and the redesigned semi-cylindrical stopper, the experimental campaign advanced toward validating the nonlinear response predicted by the numerical simulations in Chapter 3. The primary goal of this phase is to experimentally observe the transition from linear to nonlinear behavior under random and harmonic excitations, confirming the system's hardening response and the broadband energy distribution induced by contact interactions.

The theoretical framework guiding this validation is based on a detailed reference model that describes the coupled dynamics of the cantilever beam and the piezoelectric transducer under base excitation.

In this configuration, three physical quantities are directly measured during the experiments:

- Base acceleration  $\ddot{b}(t)$ , representing the input motion of the shaker table.
- Tip acceleration  $\ddot{y}(t)$ , corresponding to the absolute acceleration close to the free end of the beam.
- Voltage output v(t) generated by the piezoelectric disk.

The piezoelectric element is connected to a voltage-follower circuit that constrained the measured voltage within a safe range of  $\pm 9$  V, as previously introduced in Section 2.1.1. The electrical signal is extracted through a resistive load of R=1 M $\Omega$ , ensuring a stable and linear measurement of the voltage–current relationship within the RC circuit. The mechanical interface between the tip mass and the semi-cylindrical stopper is separated by a narrow clearance of approximately 0.5–1 mm, a critical parameter in defining the onset of nonlinear contact during the experiment.

As discussed in Section 2.2, the coupled electromechanical system can be simplified, around its first vibration mode, to a single-degree-of-freedom (SDOF) mass-spring-damper model coupled with a resistor-capacitor (RC) electrical network. The electrical dynamics can be expressed through Kirchhoff's law applied to the RC circuit:

$$v + RC_p \dot{v} - R\theta \dot{z} = 0$$

Considering the homogeneous equation and assuming  $v(t) = V_0 e^{st}$ , one obtains:

$$V_0(1 + sRC_p) = 0$$

$$s = -\frac{1}{RC_{\rm p}}$$

Indicating the presence of a single negative real pole, which defines the characteristic time constant of the RC network.

To derive the transfer function between the mechanical velocity  $\dot{z}$  and the generated voltage v, let:

$$z = z_0 e^{i\Omega t}$$
,  $\dot{z} = i\Omega z_0 e^{i\Omega t}$ ,  $v = V_0 e^{i\Omega t}$ 

Substituting into the RC equation yields:

$$V_0 + i\Omega R C_p V_0 = i\theta R \Omega z_0$$

which can be rearranged to give:

$$G_{vz} = \frac{V_0}{z_0} = \frac{i\Omega R\theta}{1 + iRCp\Omega}$$

and therefore, the magnitude of the electromechanical transfer function is:

$$|G_{vz}| = \frac{\Omega R\theta}{\sqrt{1 + (RC_p\Omega)^2}}$$

This relationship defines how the voltage output amplitude depends on the motion of the beam. As the excitation frequency  $\Omega$  increases, the transfer function magnitude approaches an asymptotic limit, see figure 4.12:

$$\lim_{\Omega \to \infty} |G_{vz}| = \frac{\theta}{\mathsf{C}_{\mathsf{p}}}$$

which represents the upper bound of the piezoelectric voltage response at high frequencies.

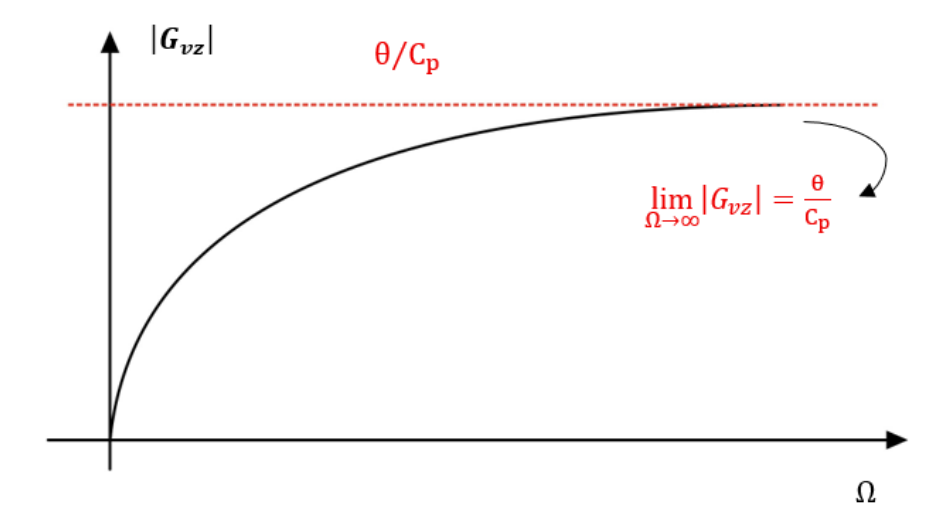


Figure 4.12: Expected transfer function about the relationship defines how the voltage output amplitude depends on the vibration frequency.

Once the theoretical transfer function  $G_{vz}$  is established, the next step is to identify the piezoelectric parameters  $C_p$  and  $\theta$  directly from the measured data. In practice, both the voltage v(t) and the acceleration response  $\ddot{z}(t)$  are recorded during each test. The velocity  $\dot{z}(t)$  is then obtained by numerical integration of the acceleration signal. From these quantities, the experimental transfer function between  $\dot{z}$  and v — denoted as  $G_{vz}$  — is estimated using MATLAB's "tfest" command, which performs a frequency-domain system identification based on input—output data.

The identified transfer function allows the extraction of the circuit parameters. The single negative pole of  $G_{vz}$  corresponds to the RC time constant of the electrical subsystem, defined as  $s = -1/(RC_p)$ . From this relation, the piezoelectric capacitance can be estimated as  $C_p = -1/(sR)$ . Once  $C_p$  is known, the coupling coefficient  $\theta$  can be computed from the high-frequency asymptotic value of the transfer function amplitude,  $|G_{vz}(\Omega^*)|$ , which tends toward  $\theta/C_p$  for sufficiently large excitation frequencies. Therefore,  $\theta$  is obtained as:

$$\theta = \lim_{\Omega \to \infty} |G_{vz}| \cdot C_p \cong |G_{vz}(\Omega^*)| \cdot C_p$$

This process provides an experimental identification of both electrical parameters, directly linking the measured electromechanical transfer to the analytical formulation introduced in Section 2.2.

After characterizing the electrical properties, the nonlinear mechanical behavior induced by the stopper is evaluated using the restoring force surface method. Starting from the simplified equation of motion

$$m\ddot{z} + c\dot{z} + kz + f_{nl}(z) + \theta V = -m\ddot{b},$$

All quantities except  $f_{nl}(z)$  are measurable from the experiments. Defining the total restoring force  $F(z) = kz + f_{nl}(z)$  and the damping term  $D(\dot{z}) = c\dot{z}$ , the equation can be rewritten as:

$$m\ddot{z} + D(\dot{z}) + F(z) = -m\ddot{b} - \theta V.$$

By rearranging terms, an equivalent restoring force surface  $R(z, \dot{z})$  can be obtained as a function of time:

$$R(z, \dot{z}) = D(\dot{z}) + F(z) = -m(\ddot{b} + \ddot{z}) - \theta V = f_{eq}(t).$$

Plotting  $f_{eq}(t)$  with respect to z and  $\dot{z}$  allows the visualization of the restoring force surface  $R(z,\dot{z})$ . Under the assumption that the damping contribution  $D(\dot{z})$  is negligible at low velocities, the elastic restoring force F(z) — and thus the nonlinear term  $f_{nl}(z)$  — can be estimated.

In the resulting F(z) - z relationship, a proportional increase of the restoring force is expected in the pre-contact region, corresponding to the purely linear response of the beam.

Considering for simplicity a symmetric gap of value equal to g, once the beam displacement reaches this value, the presence of the stopper introduces an additional contact force that causes the curve to deviate from linearity. Beyond this point, F(z) increases at a significantly higher rate with displacement, forming an upward-bending segment that clearly indicates the onset of nonlinear hardening behavior. This anticipated trend is illustrated in Figure 4.13, which schematically represents the expected F(z) - z curve derived from the restoring force estimation method.

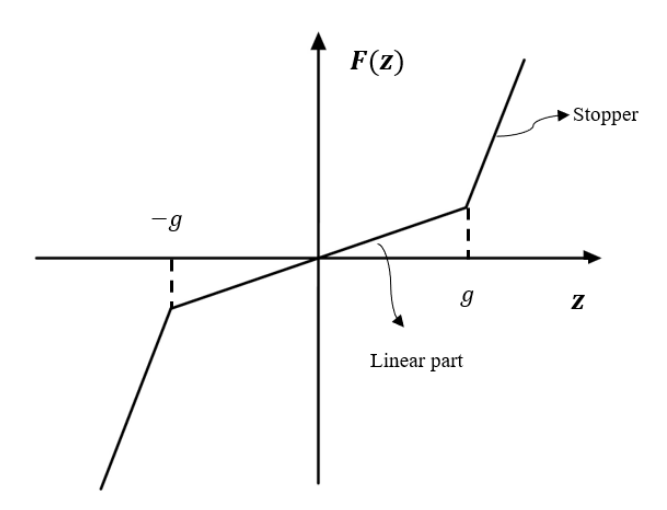


Figure 4.13: Expected restoring force—displacement relationship, showing linear behavior up to the gap and hardening response beyond contact.

From the restoring force distribution, the local equivalent stiffness can be defined as the derivative of the force with respect to displacement, which provides a more quantitative representation of the system's transition from linear to nonlinear behavior. As depicted in Figure 4.14 within the range  $-g \le z \le g$ , the stiffness K(z) remains nearly constant, corresponding to the linear stiffness of the beam. However, when the displacement exceeds the gap threshold and contact occurs, the stiffness exhibits a distinct jump to a higher plateau value, reflecting the increased rigidity introduced by the stopper. This discontinuity is a direct signature of the hardening effect, which the experiment aims to confirm through subsequent measurements.

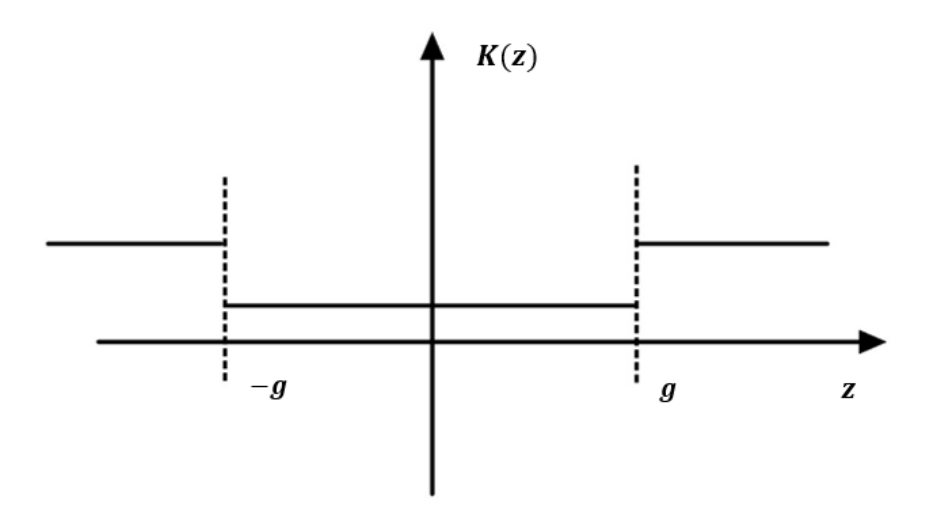


Figure 4.14: Expected equivalent stiffness distribution showing a step increase beyond the contact region, characteristic of nonlinear hardening.

These two theoretical profiles represent the anticipated mechanical response of the beam–stopper system. In the forthcoming experimental analysis, the measured restoring force and stiffness distributions will be compared against these reference trends to verify the occurrence of contact-induced nonlinearity and to assess the accuracy of the proposed model.

As mentioned above, the theoretical model identifies three measurable quantities that describe the coupled electromechanical response: the base acceleration  $\ddot{b}(t)$ , the tip acceleration  $\ddot{y}(t)$ , and the piezoelectric voltage output v(t). These quantities are recorded simultaneously and used to compute the relative motion z = y - b, the transfer functions, and the restoring-force characteristics.

Two different types of excitations are employed — random excitation and frequency-sweep excitation — to capture both broadband and amplitude-dependent nonlinear phenomena. The results are reported in the following subsections, together with the corresponding figures that illustrate the observed behavior and the parameters extracted from the data.

#### 4.4.1 Random Excitation Tests

The random excitation tests were performed to investigate the broadband dynamic response of the system and evaluate how nonlinear contact interactions influence both the mechanical and electrical domains.

The base excitation level was progressively varied from a gain of 0.5 down to 0.1, corresponding to a reduction in input base acceleration. This approach allowed a gradual transition from strong to weak excitation conditions, enabling the observation of nonlinear effects with different intensities.

Figure 4.15 displays the time-domain responses of the base acceleration, relative displacement, and piezoelectric voltage for all excitation levels. Because the base excitation is random, the three signals appear irregular and non-periodic, confirming that the applied excitation effectively excites a wide frequency band around the first natural frequency of the beam. This broadband nature ensures that nonlinear phenomena, such as intermittent contact and energy redistribution, are well represented.

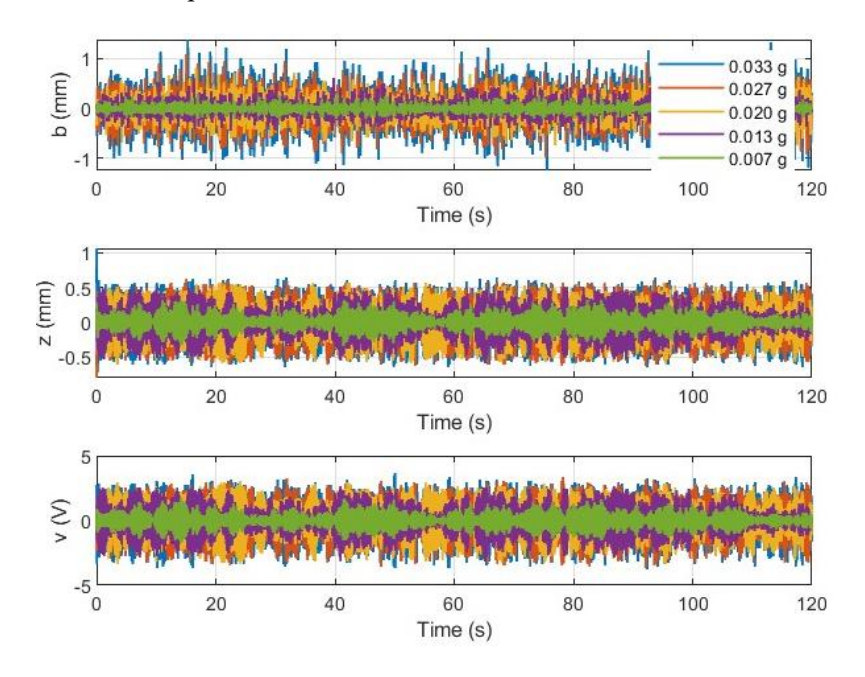


Figure 4.15 – Time-domain responses under random excitation

The frequency-domain analysis is summarized in Figure 4.16. The first and second subplots show, respectively, the relative motion over base excitation and the voltage over base excitation transfer functions. As the excitation amplitude increases (gain  $0.1 \rightarrow 0.5$ ), both transfer functions broaden and exhibit increased spectral noise, a signature of stronger contact-induced nonlinearities.

The third subplot shows the voltage-over-relative-motion transfer function,  $|G_{vz}|$ , which increases with frequency and approaches the theoretical asymptote  $\theta/C_p$ , as predicted in Figure 4.12.

This behavior confirms that the electrical coupling of the piezoelectric transducer remains stable across all input levels, and that the observed differences arise primarily from the mechanical nonlinearity of the stopper.

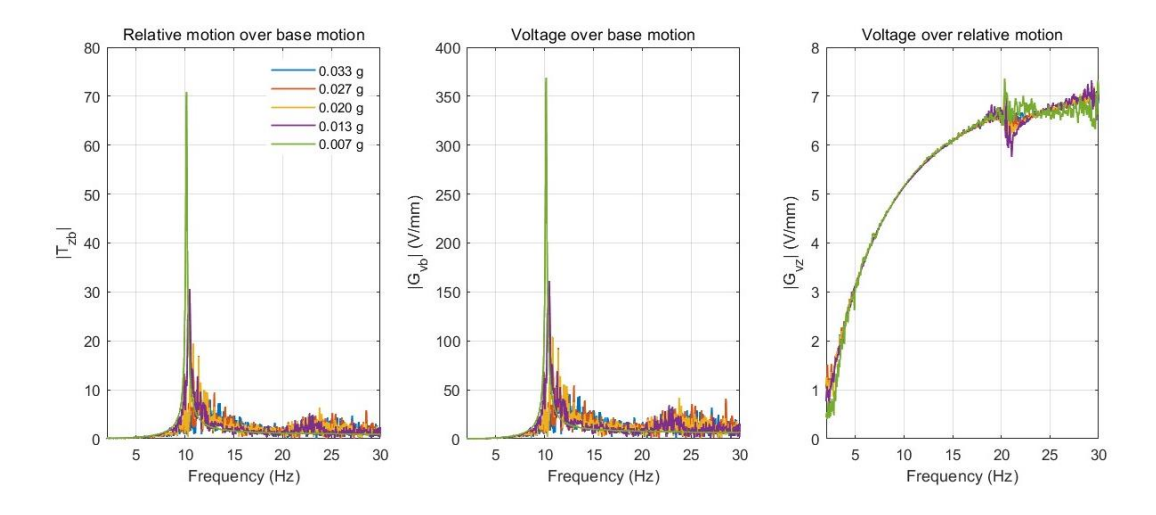


Figure 4.16 – Frequency-domain transfer functions under random excitation

The parameters  $C_p$  and  $\theta$  were identified using the frequency-response estimation procedure introduced in Section 4.5. The obtained values are shown in Figure 4.17, yielding averages of  $C_p = 14.74 \text{ nF}$  and  $\theta = 0.11 \text{ N/mV}$ , with only minor variations across different input levels. These constants are later used in the frequency-sweep analysis to calculate the restoring-force characteristics and validate the nonlinear model.

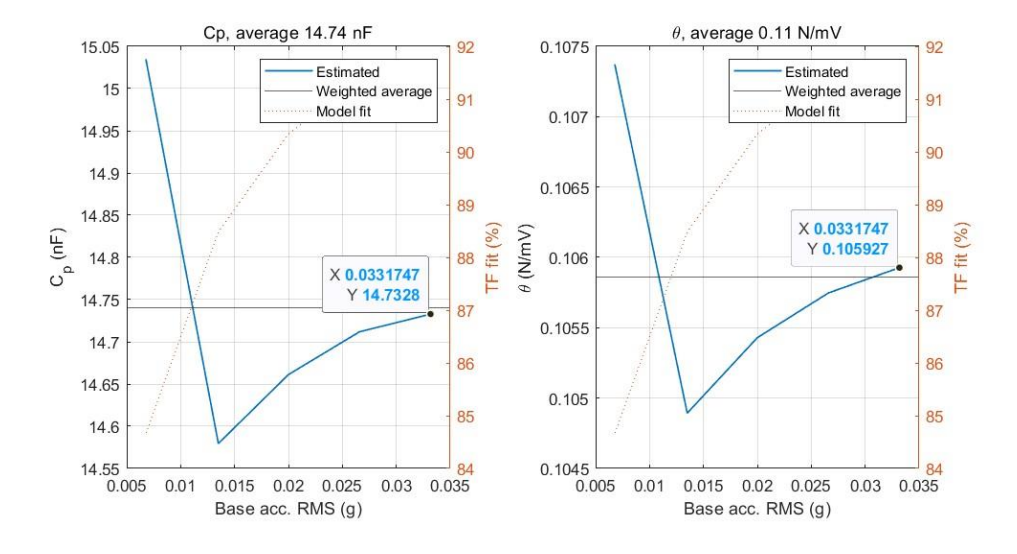


Figure 4.17 – Identification of the electrical parameters  $C_p$  and  $\theta$ 

The voltage and transfer-function characteristics are illustrated in Figure 4.18. The left subplot shows the ratio between voltage RMS and base acceleration RMS, indicating the efficiency of voltage generation under different excitation intensities.

This trend exhibits a gradual decrease beginning from the second excitation level, suggesting that as nonlinear effects strengthen, the system redistributes energy and the effective voltage output slightly diminishes.

The right subplot presents the area under the transfer function  $AUC[|G_{vb}|]$ , which first increases and then decreases with excitation amplitude, reaching its maximum at an input level of approximately 0.02 g. This specific amplitude corresponds to the optimal energy conversion condition for the designed stopper stiffness and gap configuration.

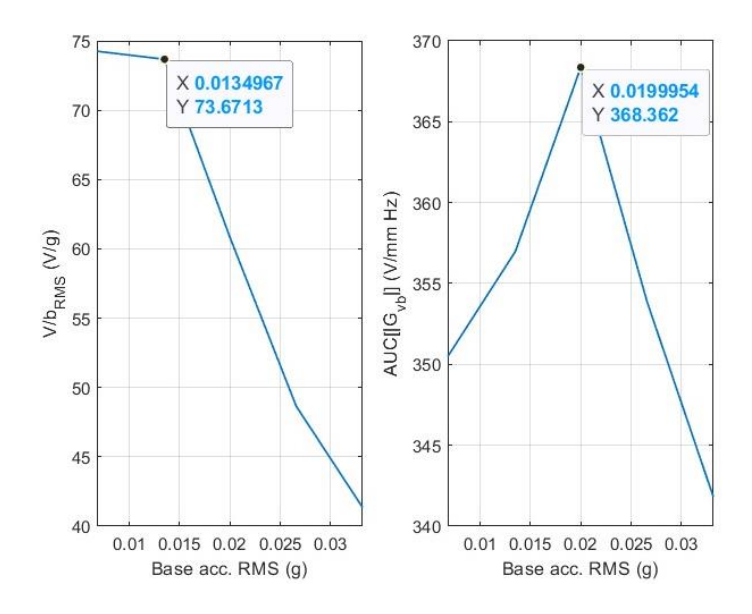


Figure 4.18 – Voltage and transfer-function characteristics under random excitation

The power analysis is summarized in Figure 4.19. The first subplot depicts the normalized instantaneous power spectrum, which shows the distribution of harvested power over frequency.

Although its overall shape varies irregularly with input level, the second subplot—average harvested power versus base acceleration RMS—reveals a clear trend: the power increases from  $40 \,\mu W/g$  at the lowest excitation (near-linear regime) to  $75 \,\mu W/g$  at 0.02 g, where the highest average power is obtained. Beyond this point, the power output decreases, indicating that excessive excitation leads to over-impact and additional losses.

This trend matches the behavior observed in Figure 4.18, reinforcing that the range between the second and third excitation levels provides the most efficient energy-harvesting condition for the designed nonlinear configuration.

This confirms that the nonlinear contact mechanism enhances the harvesting efficiency within a specific amplitude range, where impacts effectively broaden the response while maintaining stable energy conversion.

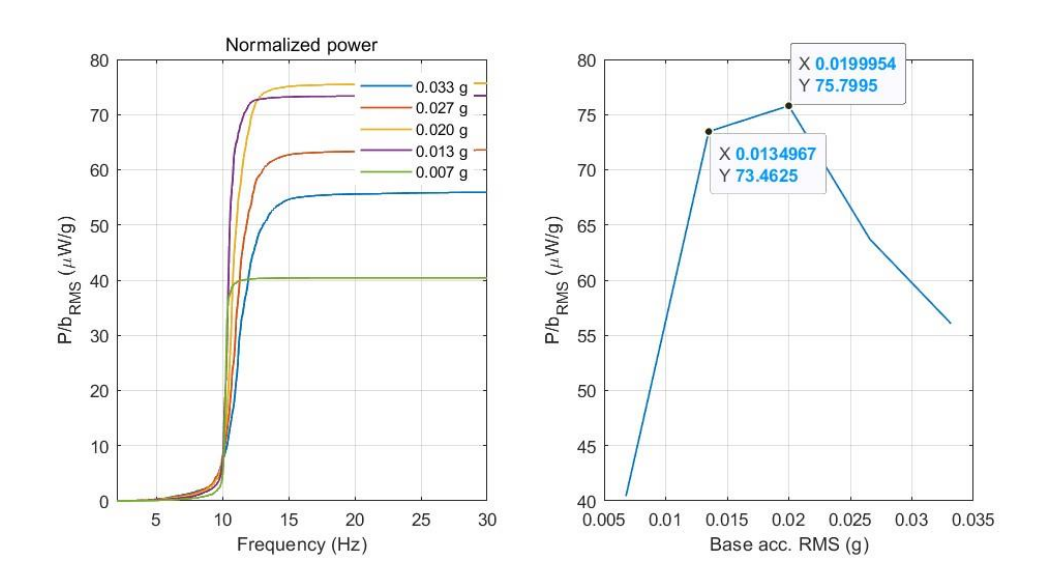


Figure 4.19 – Power generation characteristics under random excitation

#### **4.4.2 Frequency-Sweep Excitation Tests**

To complement the random excitation analysis, frequency-sweep tests were performed to evaluate the system response under controlled harmonic excitation.

Both upward (sweep-up) and downward (sweep-down) sweeps were applied around the first resonance frequency, with multiple input levels to observe amplitude-dependent effects.

Figure 4.20 show the time responses of base motion, relative displacement, and voltage during the upward frequency sweep.

As the frequency increases, the beam response exhibits pronounced nonlinear features: at low amplitudes, the motion remains nearly sinusoidal, while at higher levels the amplitude modulation and asymmetric waveform indicate repeated contact between the beam and the stopper.

The corresponding sweep-down results, shown in Figure 4.21, reveal a shift in resonance frequency typical of hardening-type nonlinearities.

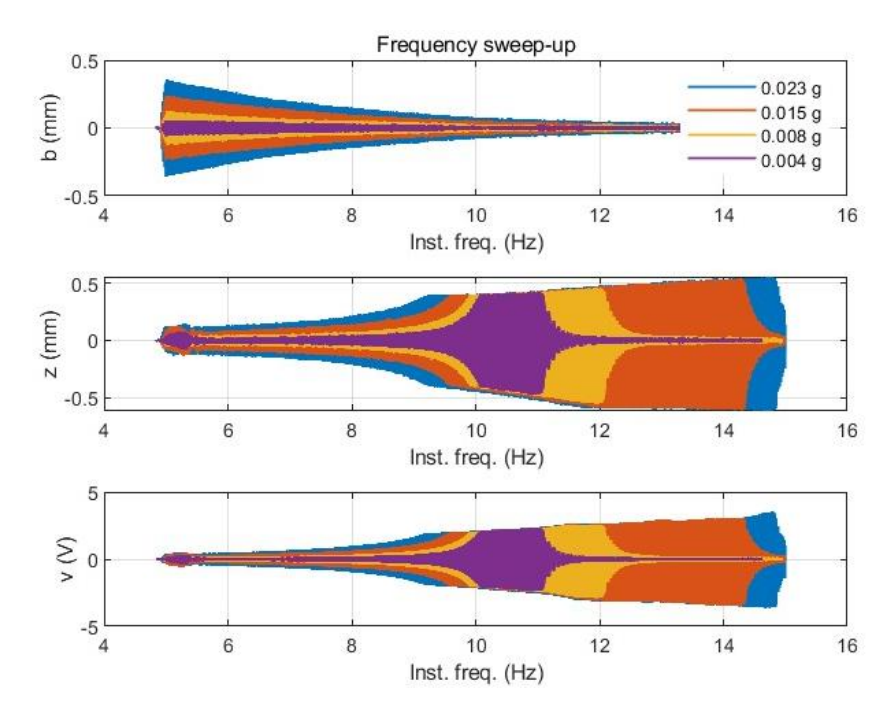


Figure 4.20 – Frequency sweep-up responses

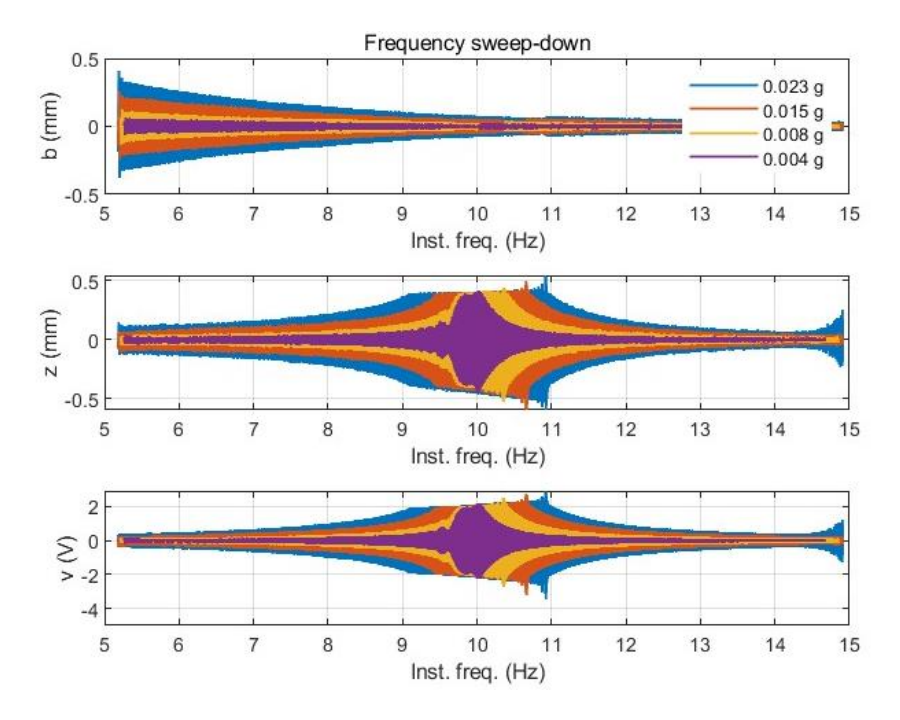


Figure 4.21 – Frequency sweep-down responses

Figure 4.22 compares the upward and downward sweeps on the same plot, showing that at small amplitudes both curves coincide, while at higher amplitudes the sweep-down curve decreases earlier than the sweep-up. Specifically, during the upward sweep, the amplitude jumps down at a certain frequency, whereas during the downward sweep, it jumps up at a different frequency—

with both jump frequencies depending on the excitation level, as shown in Figure 4.21. In fact, if the system behaves linearly there is no difference between sweep-up and sweep-down tests in principle.

This behavior confirms the hardening-type behavior predicted in the numerical simulations and demonstrates that the stopper effectively introduces the desired nonlinear contact dynamics.

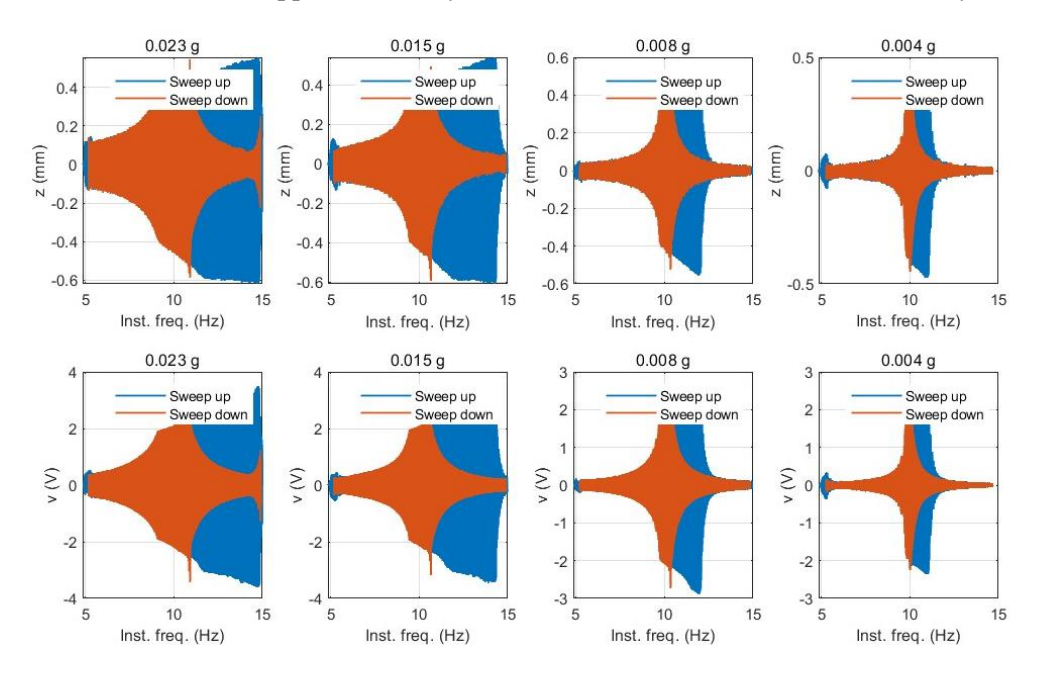


Figure 4.22 – Combined sweep-up and sweep-down responses

Finally, Figure 4.23 shows the results obtained using the Restoring Force Surface Method. The first subplot illustrates the restoring force—displacement relationship F(z), while the second shows the corresponding stiffness K(z) = dF(z)/dz.

The F(z)-z plot clearly exhibits a linear region within  $\pm 0.4$  mm, corresponding to the gap size, followed by a sharp increase beyond this range as the beam impacts the stopper. It should be noted that this measured gap is slightly less than the actual physical gap of approximately 0.5 mm because the accelerometer was mounted prior to the tip mass. Importantly, this behavior matches the expected theoretical trend described in Figure 4.13. The stiffness curve confirms a nearly constant linear stiffness in the central range and a sudden increase beyond  $\pm 0.4$  mm, indicating a transition to nonlinear contact stiffness.

Although slight asymmetries can be seen between the positive and negative sides, likely due to geometric or installation imperfections, the general behavior agrees well with the theoretical predictions.

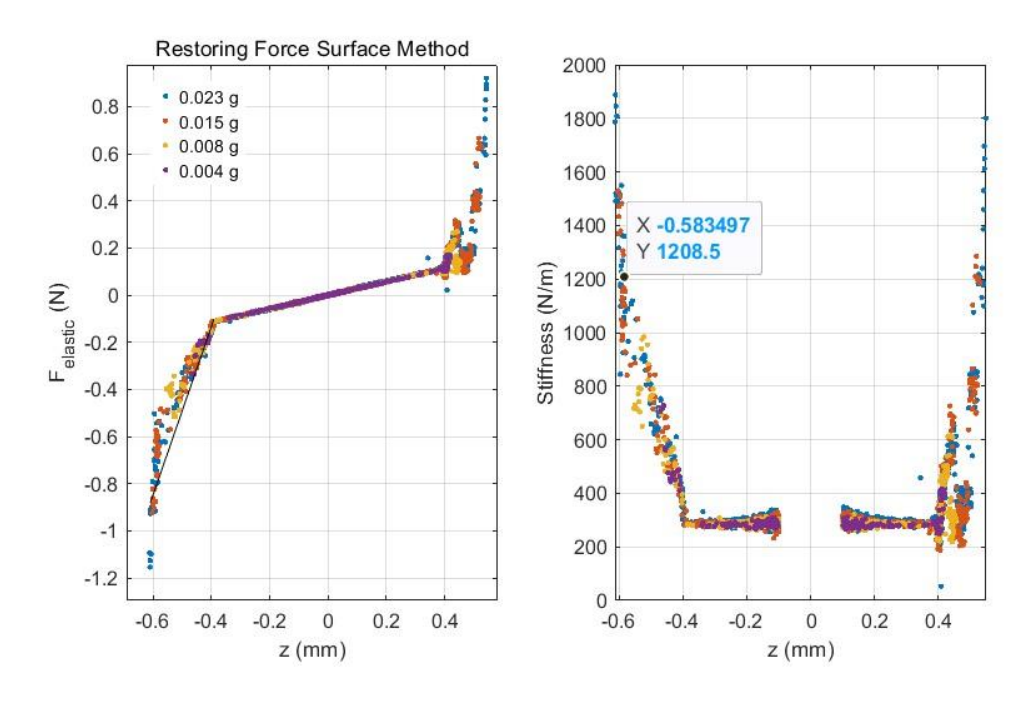


Figure 4.23 – Restoring Force Surface Method results

Additionally, from the first subfigure, the equivalent stiffness can be estimated by evaluating the slope dF/dz in the post-impact region, yielding an approximate value of 3,500 N/m. This high stiffness arises from the substantial deformation of the stopper, particularly near z = 0.6mm, where the contact force increases sharply.

In the second subfigure, a representative value for the equivalent nonlinear system stiffness can be identified around 1,200 N/m, within a broader range of approximately 1,000–1,800 N/m. This range reflects the gradual stiffness transition of the beam–stopper assembly during intermittent contact, influenced by the semi-cylindrical geometry of the stopper and the distributed deformation in the contact zone.

These quantitative estimations further illustrate the influence of the stopper geometry and deformation characteristics on the resulting nonlinear stiffness, providing a solid experimental basis for the subsequent discussion and comparison with numerical predictions.

#### 4.4.3 Discussion

The results obtained from both random and frequency-sweep excitations provide consistent and conclusive evidence of the nonlinear dynamic behavior introduced by the semi-cylindrical stopper design. Through the controlled variation of the excitation amplitude, the system response was observed to transition smoothly from linear oscillations to strongly nonlinear regimes characterized by contact-induced hardening.

In the random excitation tests, the transfer functions clearly revealed the amplitude dependence

of the response. At low excitation levels, the spectra remained narrow and well defined, consistent with a single-degree-of-freedom linear oscillator. As the excitation increased, the transfer functions broadened, the power spectrum expanded, and the voltage output began to exhibit saturation and mild irregularities—direct consequences of the beam intermittently impacting the stopper.

The estimated parameters  $C_p$  and  $\theta$  remained essentially constant throughout the entire campaign, demonstrating that the nonlinear effects originate primarily from the mechanical subsystem, while the electromechanical coupling of the piezoelectric disk remains stable. Moreover, the observed power output behavior, with a clear maximum around 0.02 g of base acceleration, highlights an optimal operating range where the mechanical contact enhances rather than limits energy harvesting efficiency.

The frequency-sweep results further confirmed these observations by providing a clearer picture of the system's amplitude-dependent resonance behavior. The divergence between the sweep-up and sweep-down responses reveals a characteristic jump phenomenon, resulting from bifurcations induced by the nonlinear stiffness hardening. This phenomenon indicates the stiffness hardening and a shift of the resonance peak towards higher frequencies with increasing excitation.

Finally, the restoring-force and stiffness plots provided direct experimental evidence of the intended nonlinear characteristics: within the  $\pm 0.4$  mm gap range, the restoring force behaved linearly, while beyond this threshold, it increased sharply as the beam contacted the stopper.

The corresponding stiffness K(z) displayed a sharp discontinuous rise beyond the  $\pm 0.4$  mm gap range. Within the linear region, its value remained close to theoretical linear stiffness, confirming consistent behavior of the cantilever. Once the beam contact with the stopper, however, local deformations at the contact interface caused a rapid increase in stiffness rather than a fixed constant value, as initially expected. This behavior—where K(z) steeply rises after the contact threshold—reflects the progressive hardening effect induced by structural deformation. The stiffness values can be interpreted directly from the restoring-force plot, where the slope dF/dz represents the equivalent stiffness of the nonlinear system.

Overall, these results validate the redesigned stopper configuration and the theoretical framework developed earlier. The combination of experimental methods—random broadband excitation for global identification and frequency-sweep testing for local jumping analysis—proved effective in characterizing the nonlinear dynamics of the system. The agreement between the observed responses and the model predictions confirms that the semi-cylindrical stopper design successfully achieved the intended motion-limiting and stiffness-enhancing effects without compromising the electromechanical performance of the piezoelectric transducer.

## 5. Conclusion

This work presented a comprehensive investigation on the nonlinear dynamics and energy harvesting performance of a piezoelectric cantilever beam equipped with mechanical stoppers. The study combined theoretical modelling, numerical simulations, and experimental validations to explore how geometric and electromechanical nonlinearities affect the energy harvesting capability of piezoelectric systems.

In the initial phase of this work, a single-degree-of-freedom (SDOF) lumped-parameter model was developed to describe the coupled electromechanical behavior of a piezoelectric cantilever equipped with motion limiters. The system dynamics were formulated in the state-space framework, enabling the inclusion of piecewise restoring forces to represent the nonlinear contact with the stoppers. However, due to the inherent discontinuities in the nonlinear terms, this approach failed to achieve convergence in some high-amplitude cases. To overcome this limitation, the Newmark–β integration method was subsequently implemented, providing a numerically stable solution for the strongly nonlinear response and allowing an accurate estimation of the system's transient dynamics. Through this approach, the influence of stopper position and stiffness on the beam's vibration response and energy conversion efficiency was systematically investigated. The simulations identified an optimal stopper stiffness of approximately 2,600 N/m, associated with enhanced power output and a frequency close to 30 Hz, confirming the theoretical benefits of introducing controlled nonlinearity.

The experimental campaign was then carried out to validate these numerical predictions and examine the nonlinear behavior under realistic operating conditions. The first prototype, equipped with vertically mounted 3D-printed stoppers, demonstrated the feasibility of the nonlinear contact mechanism but failed to reproduce the desired hardening effect due to excessive flexibility of the printed resin and gravitational misalignment. Learning from these limitations, the setup was redesigned into a horizontal configuration, featuring a semi-cylindrical stopper with higher stiffness and improved contact consistency. The second experimental phase successfully confirmed the expected nonlinear characteristics—such as the amplitude-dependent frequency shift and the hardening-type restoring response once the beam engaged the stopper. Moreover, the restoring-force surface method effectively reconstructed the nonlinear stiffness evolution, revealing a sharp stiffness increase beyond the nominal gap, in close accordance with the theoretical model.

The restoring-force analysis demonstrated that the experimentally derived stiffness values represent the global dynamic stiffness of the beam-stopper assembly rather than the intrinsic stiffness of the stopper alone. From the F-z curve, the post-impact slope yielded a local tangent stiffness of approximately 3,500 N/m, corresponding to the instantaneous contact stiffness of the entire system under full compression. By subtracting the linear beam stiffness

( $\approx$  305 N/m) from this combined response, the actual stiffness contribution of the stopper itself can be estimated at roughly 3,200 N/m. This value closely reflects the intrinsic nonlinear behavior of the limiter element, while the K-z curve provided a representative equivalent nonlinear stiffness of about 1,200 N/m (within 1,000–1,800 N/m), describing the averaged restoring properties during repeated contact and separation. The difference between these two values stems from the measurement conditions: the former captures the short-duration local stiffness at full impact, whereas the latter represents the effective steady-state stiffness of the oscillating system.

The numerically optimized stopper stiffness from the simulation model was 2,600 N/m, while the FEA-based static analysis of the redesigned semi-cylindrical stopper predicted a stiffness of approximately 3,260 N/m, obtained by applying a 1 N static force at the contact point and measuring the resulting displacement. The strong correspondence between the experimental estimate ( $\approx$  3,200 N/m) and the FEA prediction ( $\approx$  3,260 N/m) confirms that the fabricated stopper operated near the targeted stiffness range. Minor deviations can be attributed to the beam's compliance, assembly tolerances, and gradual contact transition introduced by the semi-cylindrical geometry. Overall, these findings validate both the mechanical design and numerical modelling, demonstrating that the redesigned configuration successfully reproduced the desired nonlinear hardening behavior and maintained close consistency between simulation and experiment.

In summary, the study demonstrated that incorporating mechanical stoppers can effectively induce controllable nonlinearities that enhance the broadband response of piezoelectric energy harvesters. The combination of numerical and experimental results confirmed that the nonlinear design approach is valid and predictable, providing a foundation for future optimization.

Future work may focus on refining the mechanical tolerances of the stopper mechanism, introducing adjustable stiffness control, and integrating real-time feedback for adaptive tuning. Moreover, extending the model to include multi-mode coupling and damping nonlinearities could further improve the prediction accuracy and broaden the operational bandwidth of the system.

# 6. Reference

- Wei C, Jing X. A comprehensive review on vibration energy harvesting: Modelling and realization. Renewable and Sustainable Energy Reviews [Internet]. 2017 Jul [cited 2025 Jun 10];74:1–18. Available from: https://linkinghub.elsevier.com/retrieve/pii/S1364032117300837
- 2. Ahmed R, Mir F, Banerjee S. A review on energy harvesting approaches for renewable energies from ambient vibrations and acoustic waves using piezoelectricity. Smart Mater Struct [Internet]. 2017 Aug 1 [cited 2025 Jun 10];26(8):085031. Available from: https://iopscience.iop.org/article/10.1088/1361-665X/aa7bfb
- Hussain A, Cheng W, Cao J, Du R. Numerical analysis and experimental validation of nonlinear broadband monostable and bistable energy harvesters. Communications in Nonlinear Science and Numerical Simulation [Internet]. 2024 Apr [cited 2025 Oct 10];131:107808. Available from: https://linkinghub.elsevier.com/retrieve/pii/S1007570423007293
- 4. Farhan M, Muthalif AGA, Ali MSM. Innovative approaches to optimize vibration energy harvesting (VEH): A comprehensive review. Energy Reports [Internet]. 2024 Dec [cited 2025 Jun 10];12:5194–219. Available from: https://linkinghub.elsevier.com/retrieve/pii/S2352484724007248
- Tran N, Ghayesh MH, Arjomandi M. Ambient vibration energy harvesters: A review on nonlinear techniques for performance enhancement. International Journal of Engineering Science [Internet]. 2018 Jun [cited 2025 Jun 10];127:162–85. Available from: https://linkinghub.elsevier.com/retrieve/pii/S0020722517327830
- 6. Xie XD, Wu N, Yuen KV, Wang Q. Energy harvesting from high-rise buildings by a piezoelectric coupled cantilever with a proof mass. International Journal of Engineering Science [Internet]. 2013 Nov [cited 2025 Jun 10];72:98–106. Available from: https://linkinghub.elsevier.com/retrieve/pii/S0020722513001080
- Wang H, Tang L. Modeling and experiment of bistable two-degree-of-freedom energy harvester with magnetic coupling. Mechanical Systems and Signal Processing [Internet]. 2017 Mar [cited 2025 Jun 10];86:29–39. Available from: https://linkinghub.elsevier.com/retrieve/pii/S0888327016303971
- 8. Wang L, Zhang Y, Liu S, Zhao LC, Hu KM, Li Z, et al. Enhanced vibration energy harvesting of magnetically coupled piezoelectric cantilever beam with double-point stopper. Mechanical Systems and Signal Processing [Internet]. 2025 Jun [cited 2025 Jun 10];233:112791. Available from: https://linkinghub.elsevier.com/retrieve/pii/S0888327025004923
- 9. Zhao Y, Mi X, Yin C, Chen M, Wu H. Nonlinear vibration energy harvesting-suppressing simulating and experimental research of a two-layer beam system by utilizing a vibration

- energy harvesting-suppressing module. Mechanical Systems and Signal Processing [Internet]. 2025 May [cited 2025 Jun 10];231:112731. Available from: https://linkinghub.elsevier.com/retrieve/pii/S0888327025004327
- 10. Daqaq MF. On intentional introduction of stiffness nonlinearities for energy harvesting under white Gaussian excitations. Nonlinear Dyn [Internet]. 2012 Aug [cited 2025 Jun 10];69(3):1063–79. Available from: http://link.springer.com/10.1007/s11071-012-0327-0
- 11. Gong L, Zhang G, Gao P, Wu R, Wang G, Qu Y. Tunable nonlinear piezoelectric metabeams for multimode vibration suppression. International Journal of Mechanical Sciences [Internet]. 2025 Jun [cited 2025 Jun 10];295:110238. Available from: https://linkinghub.elsevier.com/retrieve/pii/S0020740325003248
- 12. Fan Y. Ambient Vibration Energy Harvesting.